Mon. Not. R. astr. Soc. (1973) **163**, 291–322.

THE ULTRA-VIOLET SKY-SURVEY TELESCOPE IN THE TD-1A SATELLITE

A. Boksenberg, R. G. Evans, R. G. Fowler, I. S. K. Gardner, L. Houziaux, C. M. Humphries, C. Jamar, D. Macau, D. Malaise, A. Monfils, K. Nandy, G. I. Thompson, R. Wilson and H. Wroe

(Received 1973 February 27)

SUMMARY

The European satellite TD-1A was launched in March 1972 and carries, in addition to other experiments, a 27-cm ultra-violet telescope which gives low dispersion spectra over the wavelength range 1350–2550 Å and a broad band measurement centred at 2750 Å. The control system causes the telescope to scan the sky in great circles which pass through the ecliptic poles and precess by ~4 arcmin per orbit thus completing a sky survey in ~6 months. The capability of the system is such that a 9th magnitude early-type star can be detected in one scan; this limit is extended where many scans are available. The experiment is described and its performance in orbit fully assessed. Finally, a selection of reduced data extracted from quick-look magnetic tapes is presented and discussed.

1. INTRODUCTION

The European satellite TD-1A was launched from Western Test Range, California at 01·55 hr GMT 1972 March 12. The spacecraft (Tilgner 1971) carries seven experiments devoted to astronomical studies. Four of these make cosmic observations in the UV, X-ray and γ-ray regions, one measures cosmic rays and two observe solar X- and γ-rays. One of the two ultra-violet instruments (coded S2/68) was provided jointly by teams from Belgium and the UK and is the subject of this paper which describes the experiment, its performance in orbit and presents some of the early data and preliminary analysis. The instrument consists of an ultra-violet telescope feeding in turn a spectrophotometer and photometer which give low dispersion spectra over the range 1350–2550 Å and a broad band measurement centred on 2750 Å. The experiment became fully operational on 1972 March 19, on orbit 107.

The orbit of TD-1A is approximately circular in shape, of height 550 km and period 95·5 min, and is inclined at 97·55° to the Earth's equator to produce a precession of 360° yr^{-1}, or about 4 arcmin per orbit period. Thus the orbit is Sun-synchronous and tends to maintain its initial inclination of nearly perpendicular to the Earth–Sun line.

The spacecraft is fully stabilized in three axes. One axis points to the centre of the Sun with an accuracy of a few arcseconds and the perpendicular axes roll about the Earth–Sun line once each orbit. The optical axis of the telescope is aligned to one of the latter axes with the direction of view pointing away from the Earth, as shown in Fig. 1. Then, as a consequence of the Earth's motion around the Sun, the celestial sphere is scanned along ecliptic meridians, each displaced by

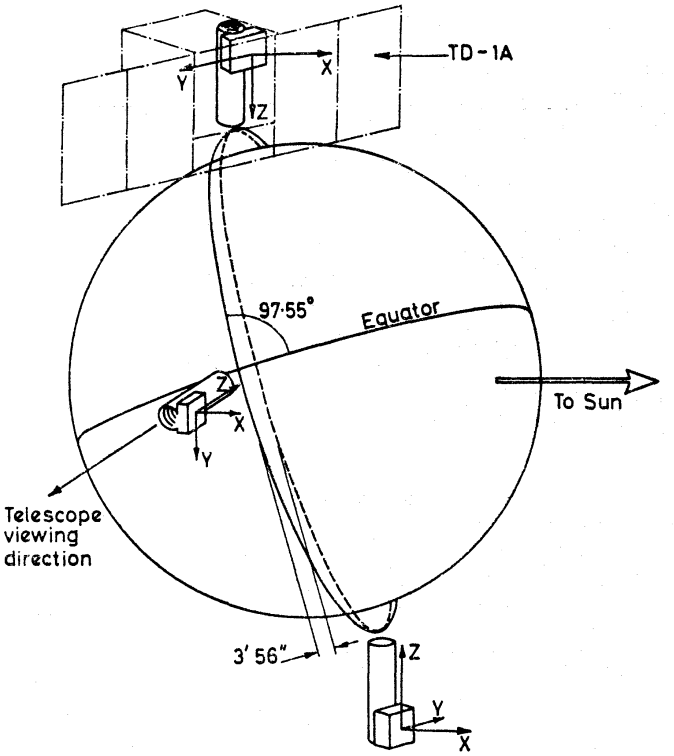

FIG. 1. *The orbit of the TD-1A satellite with a schematic of the S2/68 experiment indicating the viewing direction and the method of sky-scan.*

about 4 arcmin, and complete sky coverage is achieved in 6 months. The length of the input slots is such as to ensure three observations of objects at the ecliptic equator during successive scans; this number increases at higher latitudes and becomes large in the neighbourhood of the ecliptic poles. For a single scan, the limit of the system is about 9th visual magnitude for a B star. Because of the inclination of the Earth's equator to the ecliptic, TD-1A passes into the Earth's shadow for a part of each orbit about 7 months after launch, and stabilization is lost until subsequently the satellite is again in continuous sunlight.

2. DESCRIPTION OF THE EXPERIMENT

(a) *Concept*

A simplified representation of the optical system of the experiment is shown in Fig. 2. The telescope primary mirror is an f/3·5 off-axis paraboloid of diameter 27·5 cm. Two main slots are set in its focal plane, one for a three-channel grating spectrophotometer, the other for a one-channel photometer. Beyond the spectrophotometer slot an ellipsoidal secondary mirror directs a convergent beam to a plane grating of 1200-rulings mm^{-1}, approximately imaging the primary mirror onto it; the spectrum is formed in the focal surface of the spectrophotometer with a dispersion of 36 Å mm^{-1}. Three fixed exit slits 1 mm wide are situated in a plane close to the focal surface; behind these are three pulse counting photomultiplier detectors each illuminated by means of spherical Fabry mirrors. A similar Fabry mirror and detector also is placed behind the prime focus photometer slot.

The progressive scanning motion of the satellite causes the star images entering the telescope field to traverse the spectrophotometer and photometer slots in turn.

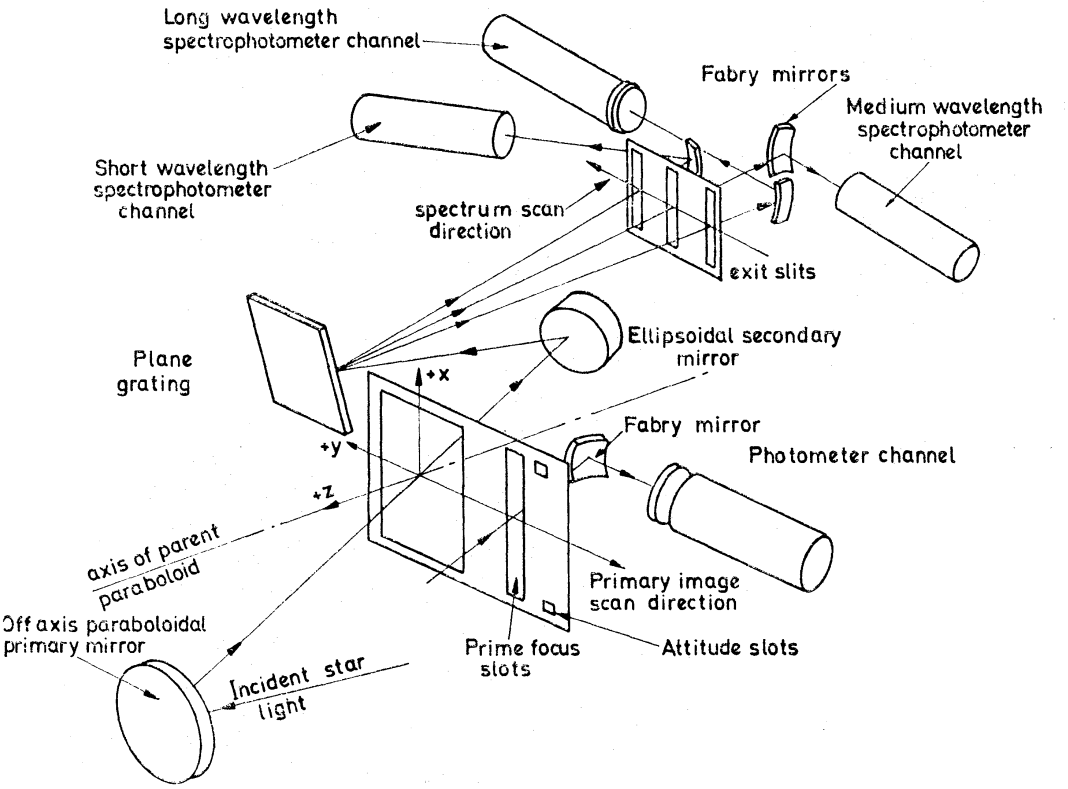

FIG. 2. *Simplified optical diagram of the S2/68 experiment—not to scale.*

The spectrophotometer slot is 11·9 arcmin wide in the direction of motion, and 17 arcmin long. The length of the slots ensures that, at the ecliptic equator, each source detected is observed unvignetted in at least three consecutive orbits. Correspondingly more repeat observations occur for sources nearer the ecliptic poles.

The traverse of a star image across the wide entrance slot of the spectrophotometer causes the corresponding spectrum image to move over the three exit slits in the direction of dispersion, thus realizing a spectrum scanning action without the need for moving parts. Referred to the entrance slot, the dispersion of the spectrophotometer is 126 Å mm^{-1}. The motion of the primary image during each detector integration interval (0·148 s) is 0·154 mm, equivalent to 19·4 Å. The effective passband during each integration interval has a full width at half height in the range 35–40 Å, depending on the channel. The wavelength range 1350–2550 Å is fully covered by the three channels in 3·3 s, yielding a total of about 60 data points. The short wavelength limit of this range was set at 1330 Å to avoid the strong ultra-violet dayglow emissions 1216 Å Ly α and 1304 Å O I; interference from the forbidden 1356 Å O I line was estimated to be negligible. Further reference is made to the day airglow emissions in the discussion of flight data below.

The passband of the photometer channel, defined by a glass transmission filter and the tube photocathode response, is centred on 2750 Å and has a full width at half height of 310 Å. Near each end of the photometer slot is an additional small 'attitude' or 'guard' slot also addressing the photometer detector. Signals occurring in these slots indicate that the primary image may be partially vignetted by the edges of the main photometer slot and by the spectrophotometer slot. The corresponding main signals are ignored when they are accompanied by a signal

from an attitude slot. The layout of the prime focus slots and a representative set of flight data illustrating the functions of the instrument are shown in Fig. 3.

(b) *Optical design*

The optical design of the instrument is the result of a very full ray tracing study carried out with the objectives of optimizing the system and providing data for the error budget. The ray tracing study also took the place of a ' bread board ' trial optical system which was prevented from inclusion in the programme by scheduling pressures. Spot diagrams were obtained of the instantaneous telescope image for a wide range of primary mirror coordinates and for many positions in the field of view, and of the instantaneous images at the exit slits of the spectrophotometer, for a wide range of slit shapes and positions. As a result of this work various refinements to the system were seen to be feasible, some of which were adopted and some not. For

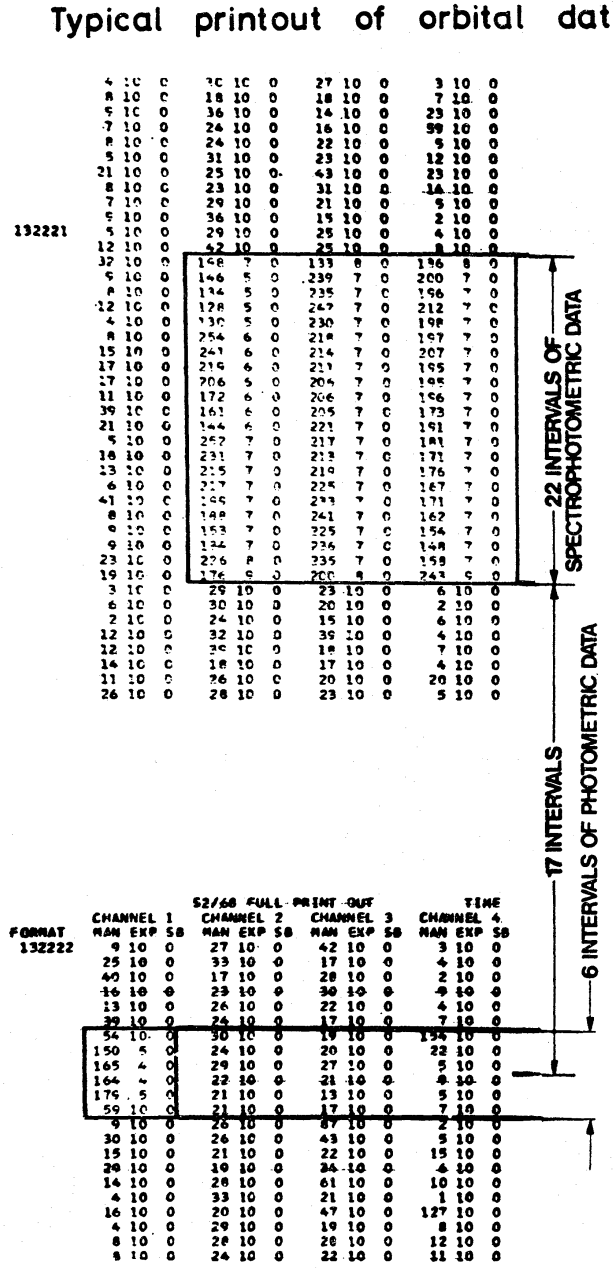

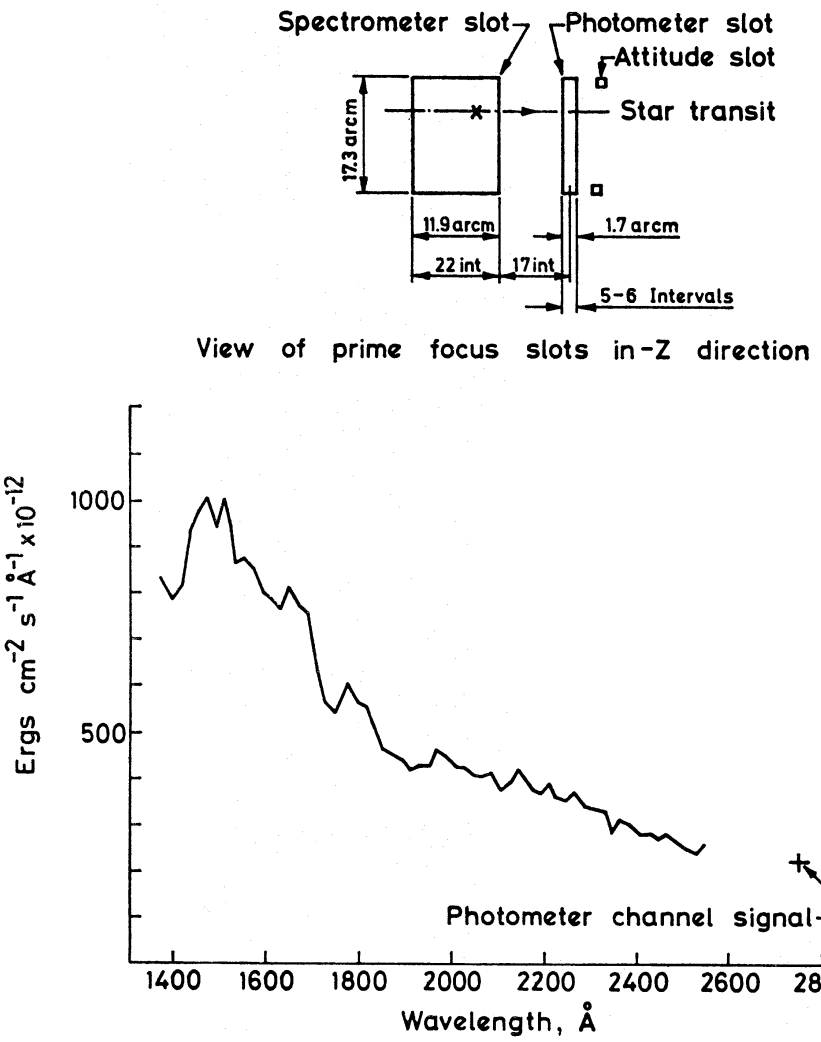

FIG. 3. *The layout and dimensions of the primary slots, together with the corresponding print-out data for the transit of γ Columbae (B3 IV, m_v = 4·35) observed on the first operational orbit* (107). *For each channel, the first column gives a mantissa A and the second column an exponent B such that the recorded count is given by* $N = A\,2^{10-B}$ *per integration interval of* 0·148 *s; the third column SB indicates when saturation has occurred by registering a one. The resulting spectrum, reduced with a preliminary calibration, is also shown. Features present include Si* IV (1394, 1403 *Å*) *and C* IV (1548, 1551 *Å*).

example, the minimum primary image width averaged over the field is obtained with the prime focus slot plate inclined from the X axis by 5·70° about the Y axis, and this feature was incorporated. On the other hand, small improvements are possible in the spectrometer by using curved exit slits and a curved slit plate. These refinements were not considered worthwhile and the final design has a plane slit plate with straight slits, the angular alignment of the plate being carefully optimized, however. Finally, the fully convoluted passbands were computed for the three spectrophotometer channels for primary image scans at various heights in the entrance slot. Some results for the medium wavelength channel are shown in Fig. 4.

The error budget for the permissible misalignments of the optics was defined by first considering the effects of displacements of perfect components by means of ray tracing and then estimating the additional effects due to real mirrors with

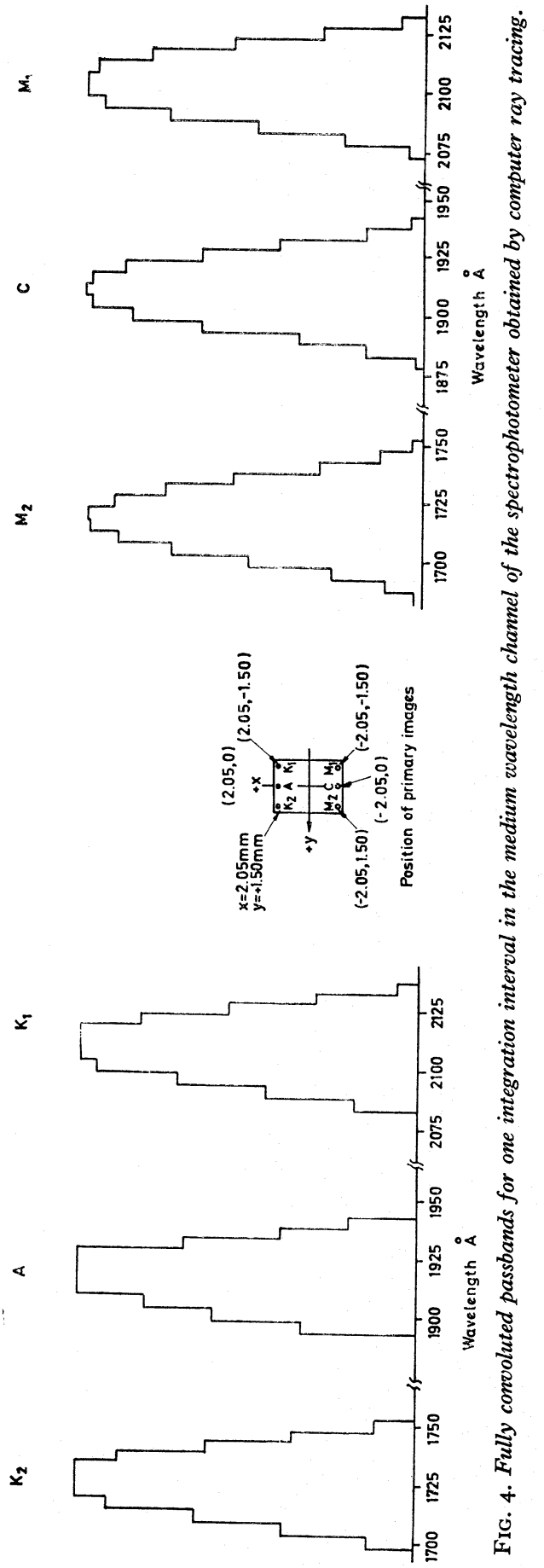

FIG. 4. *Fully convoluted passbands for one integration interval in the medium wavelength channel of the spectrophotometer obtained by computer ray tracing.*

particular image qualities. It was deduced that the spectrophotometer was not very sensitive to misalignments of its own components, except in so far as they affect wavelength register (which is calibratable) and that the major effect on spectrophotometer image quality is the change in the axial position of the primary mirror and its tilt about the Y axis. For perfect optics, the performance of the system is satisfactory if the primary mirror misalignments are such that the telescope image never exceeds about 220 μm in width anywhere in the spectrophotometer slot. This led to the adoption of telescope image size as the criterion of primary mirror alignment, i.e. the system notionally was split into two parts: primary optics and secondary optics. This is an artificial distinction and was merely adopted for convenience of constructing the error budget and performing development tests using the prime focus slot as a reference plane. For the primary optics the ray tracing was closely integrated with the mechanical design of the telescope and after several iterations a set of tolerances for the primary mirror was arrived at as follows:

Rotations about X, Y and Z axes, ± 2 arcmin.
Displacements along X and Y axes (ΔX, ΔY), ± 400 μm.
Displacement along Z axis (ΔZ), ± 500 μm.

When the above misalignments are combined in the most adverse way the primary image width at the corners of the spectrometer entrance slot does not exceed 226 μm. To allow for the effects of a real mirror a study was made of the factors affecting the image quality of the mounted mirror, including initial figuring error and distortion of the mirror by the mount. It was concluded that an inherent image width of 10 arcsec (equivalent to 49 μm in the focal plane) was feasible. The above value of allowable ΔZ then was reduced to 340 μm, which would produce a maximum image width of 177 μm with a perfect mirror. The total allowable displacements thus arrived at were apportioned between setting-up errors, shifts caused by vibration and those caused by the in-orbit thermal environment.

(c) *Baffle design*

A crucial feature of the experiment is the ability to observe faint stars while exposed to full sunlight and earthlight, and to a lesser extent, moonlight. Taking into account the respective spectral ranges and fields of the photometer and spectrophotometer and the spectra of these stray light sources, the photometer is the more sensitive to stray illumination. The effective wavelengths of this channel in the context of stray light are: sunlight, 3000 Å; earthlight, 3200 Å; moonlight, 3100 Å. In order to observe stars of 9th blue magnitude without significant interference from stray light the total attenuation of sunlight, in terms of incident sunlight at the full telescope aperture, is required to exceed 10^{14}. The levels of attenuation required for earthlight and moonlight are correspondingly lower.

The design of the stray light baffle system incorporates a means of excluding direct sunlight by the use of ' diffraction baffles ' which allow only components of second or higher order diffraction (and of scattering by dust) to enter the telescope tube. Two such baffles are fitted to the spacecraft and two more to the telescope structure mounted concentric with the tube. Carefully placed baffles within the telescope tube, largely finished with 3M 401-C10 matt black paint, then further attenuate the residual stray light. As far as possible, these internal black baffles prevent the primary mirror from seeing the walls of the tube. Finally, small baffles are incorporated in the shutter assembly to limit the view at the prime focus slots

to the primary mirror only. It remains that stray light can reach the detector mainly by diffuse and near-specular reflection of the fraction incident on the primary mirror.

Careful attention was given to the question of cleanliness, baffle edge profiles including paint, and general light tightness, both for the spacecraft and the instrument. The spacecraft could not be made completely light tight so care was taken to ensure no leakage of sunlight through external joints in the spectrometer box or telescope tube. The design of all the joints which might leak was proved by extensive tests. The direct entry of earthlight into the telescope is not possible during normal observing but earthlight can enter indirectly, largely by reflection from the rear surfaces of the diffraction baffles, at times approaching eclipse near the extremes of the observing period. Lunar illumination, although much weaker than the direct illumination of the other sources, nevertheless is potentially important since, during some observing periods, direct entry into the telescope can occur.

The design of the stray light baffle system was optimized with the aid of a computational technique specially developed at University College London. This used a Monte Carlo method and involved the construction of a mathematical model of the baffle structure, related structures and optics in complete detail, into which, as a computer experiment, individual photons were introduced. The photons then move through the system, following the probabilistic laws of interaction that are sampled by the selection of numbers from a quasi-random sequence, until they are lost either by absorption, reflection back through the mouth of the telescope or by entering the detector and so forming part of the stray light throughput of the baffle system. This procedure was carried out for a large number of photons entering the baffle system, each selected from the required input distribution. The attenuation of the baffle system was then obtained from the number of photons incident on the system and the number reaching the detector. The optimum design was then arrived at by maximizing the calculated attenuation.

The large attenuation factors involved precluded any laboratory tests of the performance of the baffle system before launch. However, orbital data, presented below, shows that the required performance was fully achieved, the level of stray light being negligible.

(d) *Flight instrument*

Fig. 5 gives a general cut-away view of the flight instrument showing details of the main structure and other features of the instrument. An electrically operated light tight shutter is fitted to the wall of the spectrophotometer box in front of the prime focus slots. The experiment was launched with the shutter closed for protection during the acquisition phase of the spacecraft attitude control system. Initial venting of the spectrophotometer box during the period of rapid depressurization occurred through two light tight ports.

The primary and secondary mirrors are made of Cervit and Zerodur respectively and the Fabry mirrors, of BK7 glass. All the mirrors were coated at the Goddard Space Flight Center with 800 Å of aluminium and 350 Å of magnesium fluoride. A reflectance of over 80 per cent was achieved over the full wavelength range covered. The reflectances were monitored throughout the pre-flight preparation programme by measurements made on small plane mirrors coated together with the flight optics and subsequently kept near them at all times. No deterioration of the flight model monitor mirrors was detected as close as two weeks to the launch.

1973MNRAS.163..291B

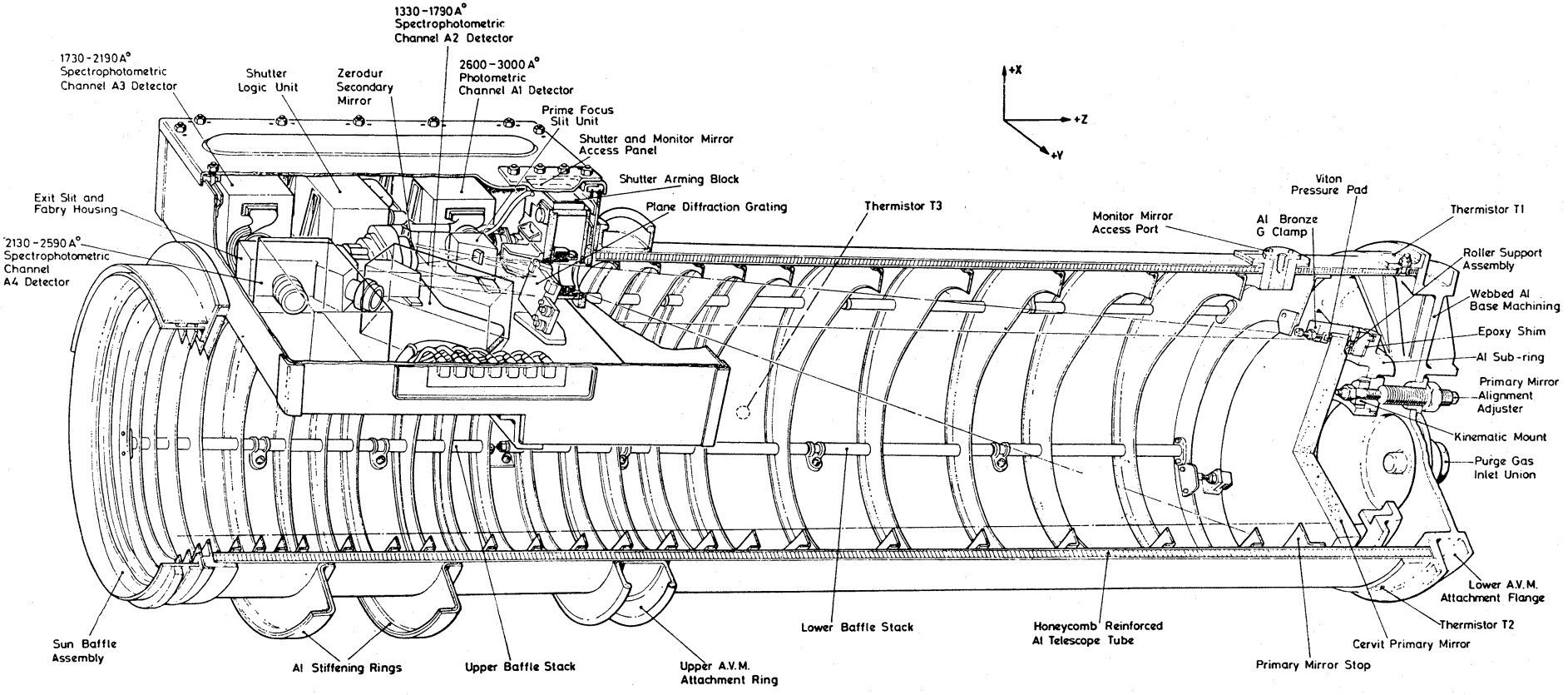

S2/68 TELESCOPE

FIG. 5. *General view of flight instrument. S2/68 telescope.*

The primary mirror is supported on a special mount having freedom to expand or contract thermally without significantly distorting the mirror itself, which has a negligible coefficient of thermal expansion. The telescope tube and the floors of the spectrophotometer box (the latter form the support for the secondary optics) are made of aluminium honeycomb. The large coefficient of thermal expansion of this structure relative to the main mirror made it necessary, when setting up and aligning the optics at the convenient temperature of 18°C, to set the primary mirror out of focus by the correct amount so that it would come into focus when the lower, orbital temperature was attained. This, in turn, led to a tight specification for the temperature distribution to be maintained in the structure of the instrument by the spacecraft thermal control system, as follows: mean temperature of telescope tube, 3 ± 5°C; transverse temperature gradient in the X (Sun) direction, ± 3°C; mean temperature of spectrophotometer box, 3 ± 3°C.

A schematic diagram of the detectors and associated electronics is presented in Fig. 6. EMR Model 542 ASCOP photomultipliers are used in all four detector channels. The photometer channel (A1), and the medium and long wavelength spectrophotometer channels (A3 and A4 respectively) all use type 542-F-08-16 having a caesium telluride photocathode and lithium fluoride window. In addition, the A4 detector has a spectrosil filter to reject the overlapping second order spectrum. The short wavelength spectrophotometer channel (A2) uses photomultiplier type 542-G-08 having a caesium iodide photocathode and lithium fluoride window. The photomultipliers are operated in a pulse counting mode with the photocathodes at spacecraft zero potential. A pre-amplifier and high voltage power supply are built into each detector unit. The pre-amplifier signals are passed to individual level discriminators, pulse shapers and counting chains. The count, N, is read out and the counter is reset every 0·150 s in each channel (the actual integration time is 0·148 s), and is coded in the binary form: $N = \mathrm{A}.2^{10-\mathrm{B}}$. This enables values of N from 0 to 524,287 to be represented by two 8-bit numbers, the mantissa A and exponent B, with a precision always better than 1 per cent. The response of each detector channel is sensibly linear up to a count rate of 10^5 per 0·148 s. Only a few of the brightest stars observed need significant correction for the effect of counting dead-time.

Magnetic shielding is incorporated in the detector units, and pre-launch tests showed that the variations in sensitivity due to the changing magnetic field encountered in orbit would be negligible. To provide adequate protection against the high energy charged particle environment in orbit it was estimated that 4 g cm^{-2} of light element shielding was needed around the photomultiplier tubes. The material of the detector boxes and spacecraft already provided this amount in all directions but that of the incident light. The necessary amount of additional shielding was provided in the form of thick walled aluminium tubing fitted in front of the detector windows and by an appropriate thickening of the spectrophotometer structure. It was not considered necessary to take steps to exclude the low energy charged particle (plasma) environment since the photocathodes are operated at spacecraft zero potential and there are no windowless detectors in the instrument.

3. INSTRUMENTAL CALIBRATION

(a) *Photometric*

An important part of the experimental preparation phase was that devoted to

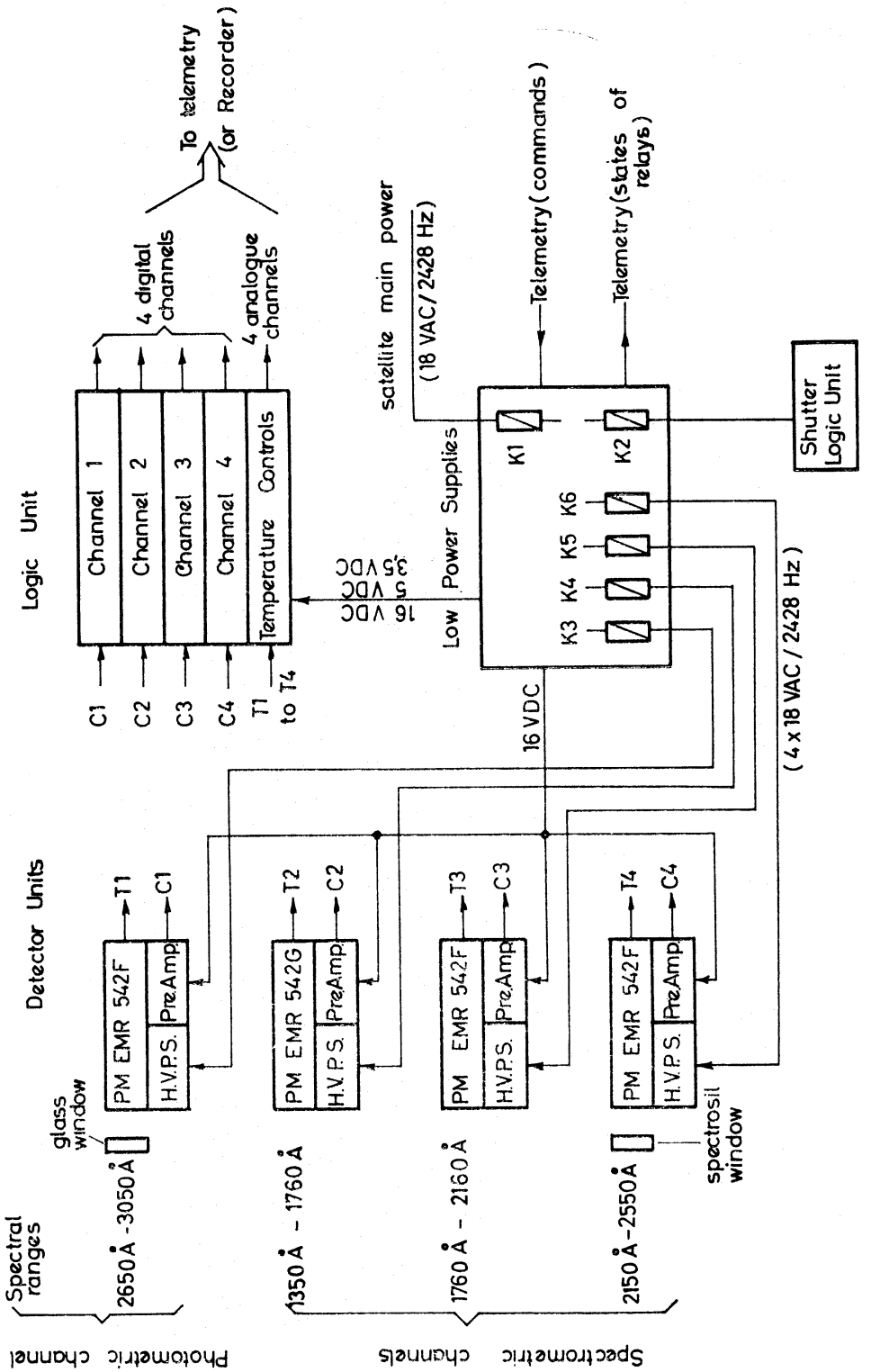

FIG. 6. *Schematic diagram of electronics.*

the photometric calibration of the instrument to allow the in-flight observations to be reduced to absolute fluxes. Since the scientific mission would benefit greatly by an absolute photometric accuracy within 20 per cent (e.g. for bolometric corrections) and from a relative photometric accuracy within 10 per cent (e.g. for colour determinations) it was decided to adopt these values as an aim and to devote considerable effort to their achievement. To this end the participating groups agreed to carry out two independent calibrations of the flight instrument, one in the UK and one in Belgium. These calibration exercises afforded an additional function in giving a complete check-out of the operation of the flight instrument under simulated orbital conditions.

The instrument calibrations were carried out at the Royal Observatory Edinburgh and the Institute d'Astrophysique, Liège. In each establishment the flight instrument was mounted in a vacuum facility which included a Cassegrain collimator fed by a vacuum ultra-violet monochromator with appropriate source. This enabled the telescope to be fully illuminated by a parallel, monochromatic beam which could be tuned through the full wavelength range of response of the instrument. The instrument was mounted on a turntable which was capable of rotating the instrument about its X-axis thus simulating the motion of the satellite and causing the telescope image to be scanned across the prime focus slots. Additional adjustment of the turntable about the Y-axis enabled the image scans to be extended to all positions along the length of the slots.

Also included in the calibration facilities was an automatic scanning device, located between the telescope and collimator, which carried a photomultiplier tube thus enabling the input beam to be fully probed and its intensity distribution determined. This photomultiplier acted as a secondary standard and was calibrated against an absolute standard in a separate exercise (see below). Hence, it was possible to determine the absolute flux of the monochromatic beam incident on the flight telescope and thereby calibrate the instrument.

Both facilities were housed in a clean room and the handling of equipment and all operations were carried out under full clean-room procedures. At Edinburgh, the measurements were made at room temperature (18 °C). At Liège, the facility had the capability of cooling which allowed measurements to be made over the temperature range -4 °C to $+18$ °C embracing the predicted orbital temperature range of $+3$ °C ± 5 °C. In addition to functional tests of the flight instrument at orbital temperature, this provided a determination of any temperature effects which may be present in the calibration.

The secondary standard photomultiplier (an ASCOP type 542 F-08-18) used in the calibration at Edinburgh was calibrated in a separate apparatus at the Rutherford Laboratory, against a windowless, vacuum thermopile. This thermopile was calibrated *in situ* in the visible against a windowed vacuum thermopile, the latter being calibrated in the visible against an absolute detector at the National Physical Laboratory. The assumption was made that the calibration of the windowless thermopile did not change with wavelength. The UV output beam from a 1-m vacuum monochromator (fed by a microwave source) was re-focused by a spherical mirror and the irradiance at this focus was measured, over a range of wavelengths, by the windowless thermopile. The large attenuation of beam intensity required for the measurement of the photomultiplier response was obtained by replacing the thermopile with a small aperture of known area and allowing the transmitted beam to diverge over a total distance of 4·5 m. At 1·2 m from the focus, the beam was

stopped down by a second small aperture. Finally, after a further 3·3 m, the beam was again stopped down by a 1 cm square aperture behind which the photomultiplier was placed. At the positions of each of the three apertures, careful measurements of beam intensity distribution were made so as to obtain accurate attenuation factors. A typical flux density at the thermopile was about 10^{11} photons cm^{-2} s^{-1} while at the photomultiplier it was about 10^{6} photons cm^{-2} s^{-1}. In order to obtain a flux at the windowless thermopile high enough for a good signal to noise ratio (about 20 : 1), measurements were restricted to 13 wavelengths at which strong emission lines occurred for the various source gases used. A few measurements were made before the calibration of the integrated instrument at ROE and many were made over a period of 6 months afterwards. No significant change was observed. This secondary standard photomultiplier was also used to transfer the absolute calibration to the secondary standard used at Liège.

Independent checks on the accuracy of calibration of the secondary standard are still being carried out. A separate calibration is being made at Liège and comparisons will be made with other standards set up in different laboratories. The full laboratory calibration exercise is therefore not complete and results presented here are based on that obtained in the UK and must be considered as preliminary.

For a given spectrophotometer channel, the in-flight pulse count for the ith integration interval, N_i, is related to the stellar photon flux. $I(\lambda)$ photons cm^{-2} s^{-1} $Å^{-1}$, by the following equation:

$$N_i = At \int_0^\infty I(\lambda)E(\lambda)T_i(\lambda)\, d\lambda$$

where $E(\lambda) = R(\lambda)q(\lambda)$ is the counting efficiency at wavelength λ, $R(\lambda)$ being the product of the mirror and grating reflectances and $q(\lambda)$ the detector photocathode quantum efficiency; $T_i(\lambda)$ is the effective exit slit transmission function for the ith integration interval; A is the telescope aperture; t is the counting interval.

To obtain $I(\lambda)$ the functions $E(\lambda)$ and $T_i(\lambda)$ are required. These were obtained in the following way. To measure $T_i(\lambda)$ a wavelength within the passband of the particular channel was set up on the monochromator, the resulting collimator beam intensity distribution was plotted and its absolute intensity derived. Next, the instrument primary image was scanned across the spectrophotometer slot by rotating the turntable, at one-tenth of the in-flight speed while maintaining the correct counting interval, and the channel response was recorded as a function of the angular position of the turntable. Measurements made over a range of wavelengths yielded the relationship between wavelength and turntable angle. This enabled the variation in channel response as a function of angle to be converted to the variation as a function of wavelength for a fixed primary image position. Fig. 7 contains a typical 'instantaneous' passband measured in this way. It must be convoluted with the primary image movement in a counting interval to obtain the effective passband for use in the above equation. The convoluted passband obtained in this way also is shown in Fig. 7 and is compared with the result obtained by computer raytracing.

Each instantaneous passband has a flat portion in the centre where light from the primary mirror passes through the optical system to the detectors without vignetting. The response at these wavelengths was used to calculate the counting efficiency term $E(\lambda)$. The variation of $E(\lambda)$ with λ is shown in Fig. 8. Measurements were taken with the primary image at several heights in the entrance slot; the

resulting variation in $E(\lambda)$ was less than 2 per cent. The adopted scan rate of one-tenth of the in-flight value reduced the uncertainty in the phase of the primary image with respect to the integration intervals from approximately $+10$ Å to ± 1 Å.

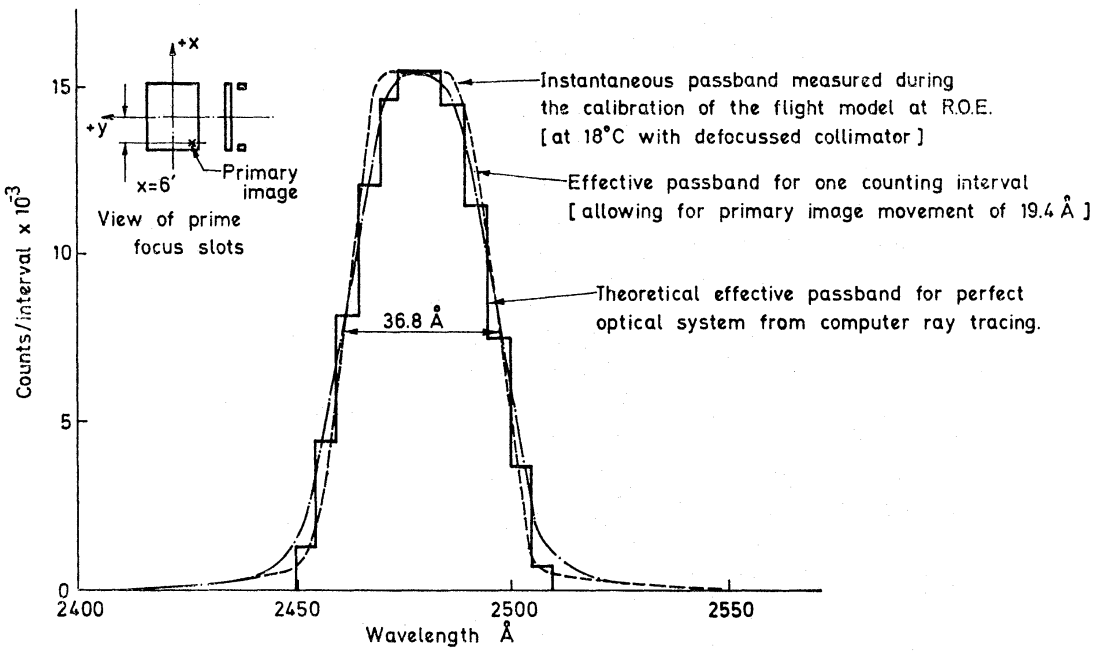

FIG. 7. *Flight model passbands near 2480 Å in the A4 channel at x = −6 arcmin.*

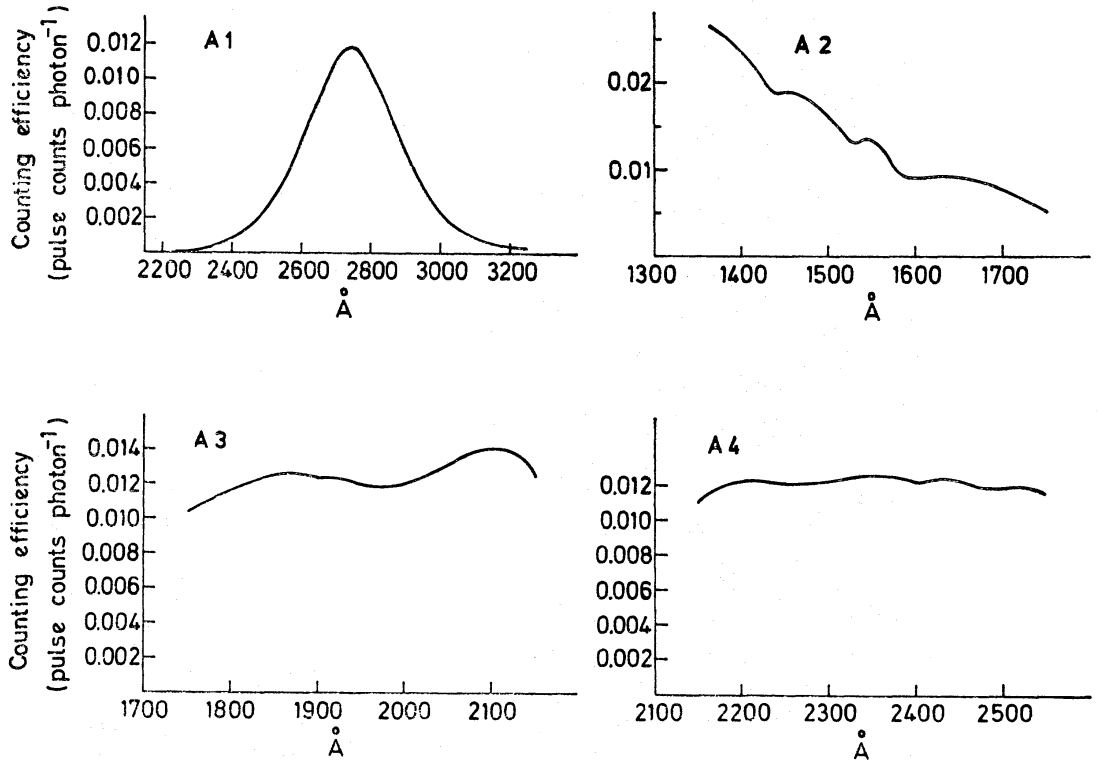

FIG. 8. *Preliminary values of instrumental efficiency, estimated accuracy within* ±20 *per cent.*

For the photometer channel, the passband is not a function of primary image position, but the slow scan method was still employed. The measured counting efficiency for an unvignetted primary image plotted as a function of wavelength is also shown in Fig. 8.

As indicated above, the full laboratory calibration and comparison of the independent measurements is not yet complete, and in addition variations with time will have to be considered. The effects of possible variations in the pre-launch phase were minimized by calibrating the flight instrument as late as possible in the programme (4–5 months before launch). Further, a check on the optics (probably the most vulnerable to variation) was afforded by small test mirrors maintained with the flight instrument. The last measurement on these, made about 2 weeks before launch, revealed no change. In orbit, variations in calibration will be checked by examining repeated observations of objects near the ecliptic poles, and of objects which are observed again when the sky-scan is completed, about 6 months after launch.

(b) *Wavelength calibration*

While an image is in the photometer slot, the observed wavelength distribution is defined entirely by the selective response of the photometric channel (Fig. 8). When a point image is in the spectrophotometer slot, the observed wavelength is a function of its position. This has been determined in the laboratory calibration procedures and related to time for an orbital scan. This wavelength scale will be re-determined using in-flight data for stars with well-defined spectral features. The problem is then to determine the zero point or moment of entry of the image into the system. This itself is linked with the problem of star identification and will be carried out as part of the data reduction task. The method is to use the signal in the photometer channel to determine the precise time of entry into the spectrophotometer slot. Since the integration intervals correspond to 19·4 Å, the phase of the read-out with respect to the slot must be determined. This is done by using the photometer response (Fig. 8) measured accurately in the laboratory with a slow scan. This enables histograms of response as a function of counting inverval to be constructed which correspond to the in-flight scan speed but with a range of relative phase. By matching similar histograms produced from orbital data, the uncertainty in the phase of the image, in orbit, can be greatly reduced. Thus the inherent uncertainty of approximately ± 10 Å in the wavelength calibration of the spectral data can be reduced to less than ± 2 Å.

4. PERFORMANCE IN ORBIT

(a) *Optical*

Degradation in the optical performance of the flight instrument can be caused by distortions induced either in the launch phase or by excursions from the prescribed temperature limits set by the experiment. The former is a mechanical problem and the structure was designed to withstand the launch environment without loss of alignment, this being checked by simulated tests in the laboratory. The latter is a thermal problem concerned with the satellite as a whole and also involved simulated laboratory tests. For an orbital check, five thermistors were built into the experiment at critical points, two in the A1 and A4 detector boxes

and the others in the telescope tube labelled T1, T2 and T3 in Fig. 5. Extensive thermal testing of the integrated spacecraft at ESTEC showed that the T3 temperature was always close to the mean tube temperature. Furthermore, an estimate of the transverse temperature gradient in the instrument X direction can be obtained by applying a simple empirical formula to the difference (T1 – T2). The telemetered values of these five temperatures show, after some initial variation, the steady state values of 1·4 °C for A1, 0·3 °C for A4, 5·7 °C for T1 and 4·1 °C for T2. The spectrophotometer box temperature, taken as the mean of the A1 and A4 temperatures, is 0·8 °C and the estimated transverse temperature difference in the X direction is 2·5 °C. These are within the respective specified ranges of 3 ± 3 °C. The mean temperature of the telescope tube, 5·6 °C as given by T3, also is within its specified range 3 ± 5 °C. These tolerances were set by the criterion of negligible optical degradation and hence the optical performance in orbit should be optimum.

A more direct check is afforded by an examination of the scientific data themselves. In particular, the signal distribution as a star image passes over the photometer slot allows the state of focus of the telescope to be tested by comparing the observed signal histogram with that computed from the laboratory measurements (see above) made at optimum focus. This histogram is not unique because of the variation in the phase of the counting interval relative to the position of the image in the slot.

Comparisons have been made for a number of observations which show that the in-flight data are indistinguishable, within the errors, from that predicted and that the phase can be determined to an accuracy of 0·1-integration interval. Two example comparisons are displayed in Fig. 9 for stars observed about one week apart. The best fit histograms shown in the figures are for phases 0·4 and 0·1, respectively. The deviations between observed and predicted histograms are comparable to the square root of the actual number of counts and are within statistical fluctuations.

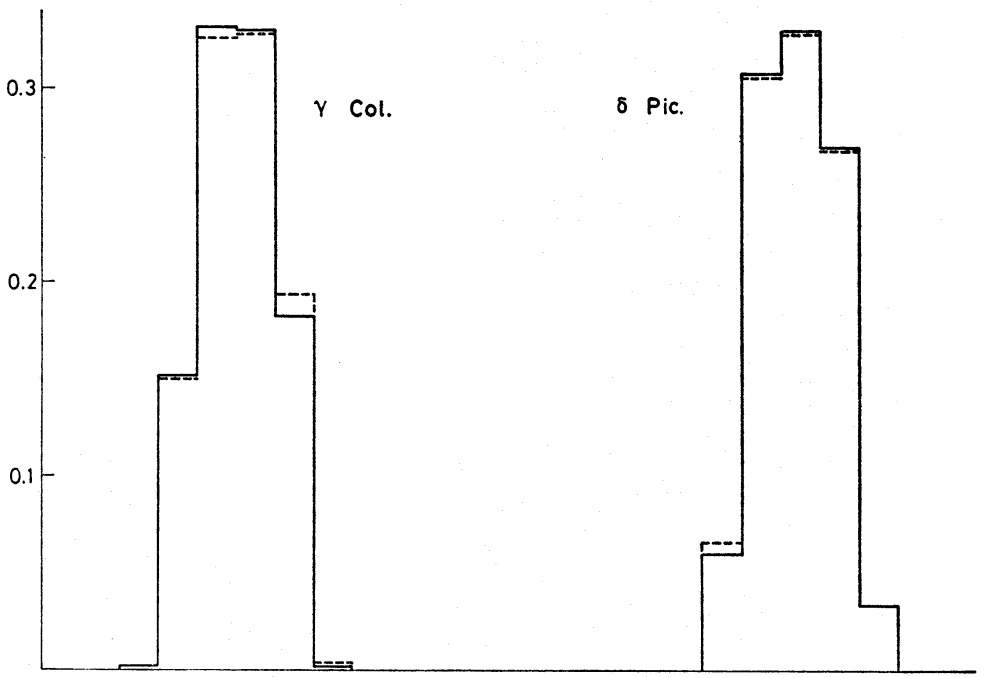

FIG. 9. *Histograms of A1 channel in-flight data compared with calibration data, both normalized to unit sum.* ———, *in orbit values;* --------, *calibration values.*

It can be concluded that the telescope is in good focus and alignment. The matching of phase will be carried out as a regular feature of the data reduction since it is important to the determination of attitude and wavelength (see below). The quality of the spectral data, showing well-defined features at the expected wavelengths, indicates that the spectrometer also is in good focus.

(b) *Background and noise*

The background signal levels, in counts per integration interval of 0·148 s averaged over 32 intervals, are plotted against telemetry format numbers (1° of latitude corresponds to about 3·3 formats) for orbit 107 in Fig. 10. The approximate positions of the geographic and galactic equators and poles are indicated. Background signals obtained in orbit 106 with the shutter closed are shown in the same figure where they are available. The scale of this background, in terms relevant to the mission, can be determined from an approximate ' calibration factor ' for the A1 channel in which a count rate of 90 per interval corresponds to an unreddened Bo star of 9th visual magnitude.

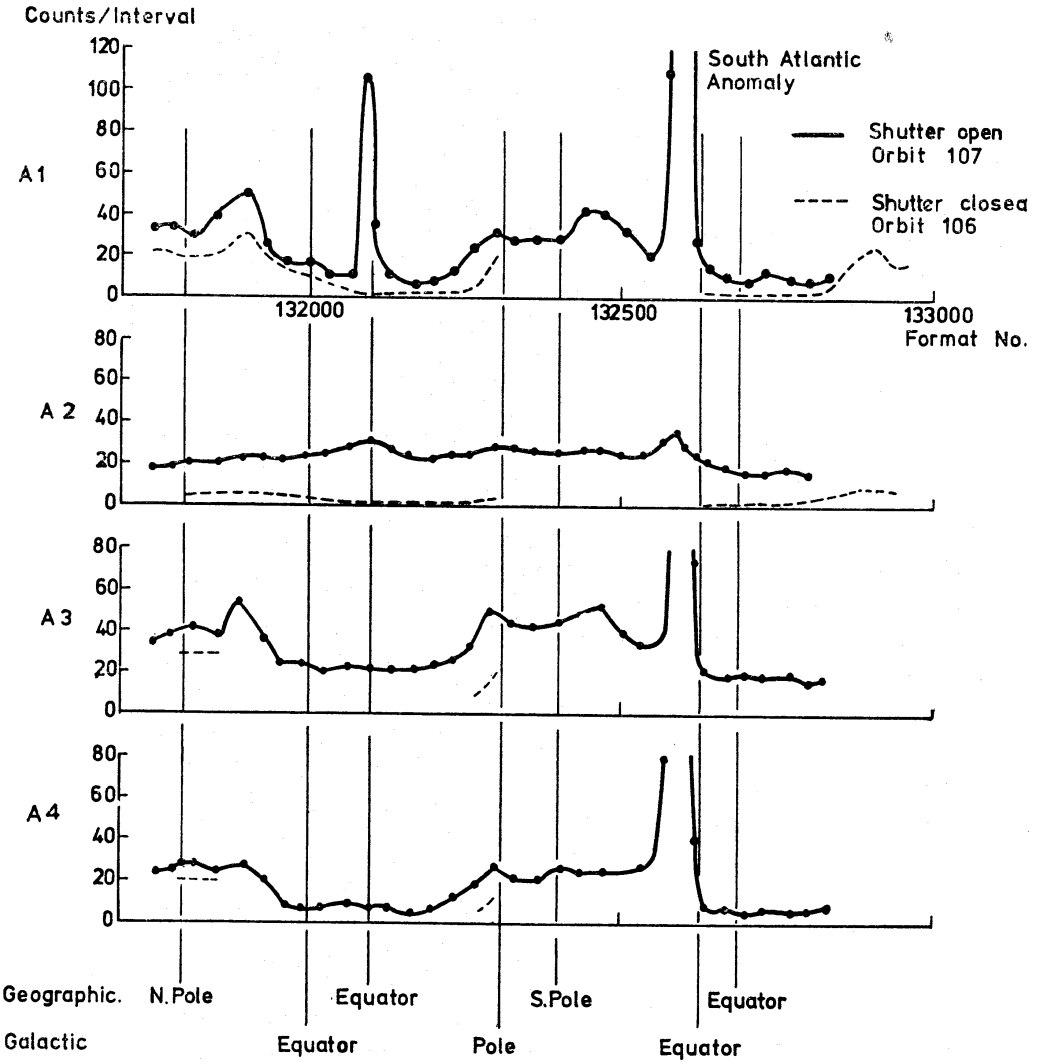

FIG. 10. *Background levels in each channel obtained by averaging over one format* (≡ 32 *counting interval*) *and excluding all identifiable stars. The channel passbands are A1, 310 Å centred on 2750 Å; A2, 1350–1760 Å; A3, 1760–2160 Å; A4, 2150–2550 Å.*

It is evident that, with the exception of the feature present in the A1 channel near the equator (discussed separately below), the background behaviour is similar in channels A1, A3 and A4. The signal varies through the orbit being low at the equator and increasing significantly in the auroral regions and particularly in the South Atlantic Anomaly through which the satellite passed during this particular orbit. This pattern reflects the changes in the charged particle environment caused by the Earth's radiation belt. The increases in background count are caused by scintillations induced in the lithium fluoride windows of the detectors by high energy charged particles capable of penetrating the shielding.

The background behaviour of channel A2 is quite different from the other three channels. The small increase of signal in the South Atlantic Anomaly is orders of magnitude below that in the other channels and indicates that A2 is essentially insensitive to particle-induced scintillations. The fact that the A2 detector is electrically identical to the other three and only differs in its photocathode material (caesium iodide as opposed to caesium telluride) indicates that the induced scintillations substantially emit at wavelengths longer than its cut-off.

We now consider the background signals in orbit 106 when the shutter was closed. In channel A1, the 106 background follows the same pattern as 107 (with the exception of the feature near the equator—see below)—but at a lower level. This confirms the conclusion that particle radiation is the main cause of background in this channel and indicates that a small UV radiation background is present at a level of about 10 counts per interval. This difference between orbits 107 and 106 does not give a precise estimate of the UV background because of the difference in the geomagnetic longitudes between these orbits, but the fact that the 107 background drops below 10 counts per interval at its lowest level supports that value as a reasonable estimate of the UV component.

Contributions to the UV background can come from star background, airglow and scattered sunlight. We are more concerned here with the third contribution since the only experimental determination of the amount of scattered sunlight that penetrates the baffle system must come from orbital data. An upper limit can be derived by assigning the full UV background in the A1 channel, estimated at 10 counts per interval, to scattered sunlight. This gives an attenuation factor of greater than 10^{14} and a stray light background which is fainter than would be produced by a B star of 11th magnitude. It can be concluded that the performance of the stray light baffle system is completely satisfactory. Further, since stray light signals in the A1 channel are orders of magnitude greater than in the other channels (due to higher solar intensity), then any contribution to background in channels A2, A3 and A4 due to stray light is completely undetectable, even on the basis of the upper limit. The fact that these channels exhibit a significant difference in signal when the shutter is open and closed shows the presence of a UV background due to some other cause, almost certainly airglow. The presence of such a component in these three channels indicates the probability of an airglow contribution to A1 which, together with a small but significant contribution from star background, would make the upper limit for scattered light an excessive one.

As indicated above, the background in the short wavelength spectrophotometric channel A2 has a quite different character from the other channels, being largely insensitive to particle radiation. The observed background is therefore dominated by ultra-violet radiation and a glance at Fig. 10 indicates that this is roughly constant at a level of ~ 20 counts per interval. The only possible candidate

for such a signal is airglow. However, the level is too high to be accounted for, at the satellite altitude, by the day airglow zenith emission 1356 Å O I, which fall within the passband. On the other hand, the signal is readily accounted for in terms of instrumentally scattered day airglow 1216 Å Ly α. Laboratory measurements of the instrument scattering in Ly α, obtained during the calibration and testing phases, gave a value of approximately 4×10^{-3} for the relative flux scattered into the A2 detector from Ly α radiation entering the spectrophotometer from anywhere in the prime focus slot. Taking the accepted value of a few kR for the 550-km zenith intensity of the Ly α day airglow, and applying the above scattering factor and the instrument parameters, gives a value for the background counting rate close to that observed.

The difference in character of the background in the four channels is reflected by the noise statistics which were investigated by determining from data blocks of 256 points the mean signal M and its mean square deviation D. In the case of the A2 channel, the background is consistent with Poisson statistics ($\log D = \log M$) as would be expected from a photon signal. In the case of the other three channels, A1, A3 and A4, the fluctuations are much larger than would be given by a Poisson distribution and are represented by $\log D = 1{\cdot}75 \log M$. This is obviously due to the nature of the background in these channels which is caused by high energy particles. The induced phosphorescence must then provide a varying number of counts within the integration interval of the system. The different types of noise statistics give an additional method of distinguishing between photon and particle-induced signals.

The feature which remains to be explained in the background plots of Fig. 10 occurs in the photometer (A1) channel near the equator on orbit 107 (and sporadically on subsequent orbits). Its near absence in channels A3 and A4, together with its noise characteristics, establishes it clearly as a photon signal. The feature extends over $\sim 20°$ and has a peak intensity (~ 100 counts per interval) which corresponds approximately to a 9th magnitude B star. The satellite includes a second ultra-violet experiment (S59—provided by the University of Utrecht) which observed directly corresponding signals although its direction of view was 8° away at the time of detection. This rules out the feature as emission from an astronomical object. Several other possibilities were investigated and also ruled out, among them: sunlight reflected off local debris or an ejected portion of the spacecraft; moonlight entering the telescope tube; sunlight locally scattered from gas released during the frequent periods of momentum unloading. After considerable investigation the feature has been identified as being atmospheric in origin (Boksenberg & Gerard 1973). When seen it is localized near the magnetic equator and has an extent of a few thousand kilometres. The signal is attributed to resonance scattering of sunlight by singly-ionized magnesium ions in a column above 550 km. The conclusions confirm previous mass-spectrometric measurements (Hanson & Sanatini 1970) in the equatorial ionosphere and are generally consistent with the vertical transport mechanism proposed by Hanson, Sterling & Woodman (1972) and others.

(c) *Signal identification and attitude solution*

A basic problem in the data reduction procedures is the determination of the celestial coordinates corresponding to an observed signal and its subsequent identification with an astronomical object. The data reduction programme detects

star signals automatically by convoluting the telemetry data with a filter which approximates the shape of the expected signal and eliminates the mean local background. Both A1 and A2 channels are searched in this way, the filter being five integration intervals wide in A1 and 22 integration intervals wide in A2. Due to the ' noisy ' background the threshold for detection of star signals in A1 is larger than for A2. The A1 data points are fitted to a parabola and its apex gives the position and strength of the signal. Where necessary, a similar procedure can be applied to A2.

Star identification is performed with the aid of a catalogue, compiled at the University of Mons, which was formed by selection from the SAO and includes B types down to $m_v = 9$, A types to $m_v = 8$ etc. It is arranged in ecliptic coordinates for which the equations of motion of the telescope axis are quite simple, as it is moving nearly in a great circle of constant longitude with latitude changing linearly with time. The departure from the great circle is due to the orbital precession which changes the longitude by 4 arcmin per orbit.

Strong signals are easily identified using the approximate pointing direction supplied by the European Space Operations Centre from spacecraft sensor data. The positions of the identified stars are then used to determine the constants β_0, β_1 in the equation $\beta = \beta_0 + \beta_1 T$, where β is the ecliptic latitude of the telescope axis and T is the time from an arbitrary origin. It is found that the satellite scan motion is extremely steady and perturbations need not be considered. The mean square deviation of the computed latitude from the true latitude for these bright stars is only 5 arcsec, equivalent to 0·14 integration period. When this linear relation has been set up even quite faint stars ($m_v = 9$ at late B) can be identified.

The longitude solution is not as accurate as the latitude solution because of the slot length and any signal which does not also appear in the ' attitude ' slots is only located to within $\pm 7{\cdot}5$ arcmin. The method of solution adopted is to start with the longitude given by the spacecraft Sun sensor and to predict the occurrence of signals through an orbit, together with their estimated distance from the slot centre. Any absent signals then give an estimate of a minimum correction to be applied to the longitude solution. Additionally, when a signal is present in one of the attitude slots, its identification locates the longitude to within $\pm 0{\cdot}5$ arcmin and consequently is given high weight in the solution.

The above method of extracting stellar signals, the determination of the corresponding celestial coordinates and subsequent identification was fully tested on a quick-look tape covering orbit 227. Eighty-three stellar signals were detected, 81 using the A1 channel and two using the A2 channel in the South Atlantic Anomaly when the A1 background was high. Of the 83 signals, 73 have been positively identified with stars in the SAO catalogue. The faintest of these has $m_v = 9{\cdot}5$ with no SAO spectral type listed and the latest spectral type is K0 with $m_v = 5{\cdot}6$. Four of the identified stars are brighter than $m_v = 5{\cdot}0$ and 30 are fainter than $m_v = 8{\cdot}5$. Ten detected stellar objects remain unidentified, the strongest giving a total signal of 310 counts in the A1 channel which would correspond to $m_v \sim 9$ if the object is a B star.

5. EARLY RESULTS

(a) *Stellar observations*

Data recorded by the UV telescope during the first few weeks after launch have been analysed to obtain absolute measurements of stellar flux. Observations of

stars as faint as $V = 9{\cdot}5$ have been obtained, but the present selection is restricted to $V \leqslant 7{\cdot}0$ and includes a number of bright unreddened stars which have been used to study the intrinsic ultra-violet colours over a wide spectral range. As described above the spectra are sampled at 19·4 Å intervals by a three channel grating spectrophotometer which covers the wavelength range 1350–2550 Å with a passband of width 25 Å at half maximum and by a photometric channel with passband centred at 2750 Å of width 310 Å at half maximum.

The data presented here were derived from a set of quick-look magnetic tapes covering 50 orbits. Since the orbits contained on these tapes were not consecutive, only one set of measurements was available for most of the stars. The complete set of consecutive data tapes will have generally at least three sets of measurements for each star.

Table I lists the reddened and unreddened stars which have been selected for this investigation, together with their spectral type, V magnitude and $B-V$ colours. The absolute monochromatic fluxes $I(\lambda)$ (in erg cm^{-2} s^{-1} Å^{-1}) have been determined at 62 wavelengths using the preliminary calibration and procedure described above and reduced to ultra-violet colour indices defined as:

$$m(\lambda) - V = -2{\cdot}5 \log_{10} \frac{I(\lambda)}{I_{5480\text{A}}}$$

where $I_{5480\text{A}} = 3{\cdot}64 \times 10^{-9}\ 10^{-0{\cdot}4V}$ erg cm^{-2} s^{-1} Å^{-1}, after Oke & Schild (1970). The present primary concern is with the relative intensity distribution of stars and, hence, Vega has been adopted as a standard and relative ultra-violet colours are defined as

$$U(\lambda) = (m(\lambda) - V)_{\text{star}} - (m(\lambda) - V)_{\text{Vega}}.$$

Fig. 11 illustrates the relative flux distribution for a range of spectral type using a selection of unreddened stars from Table I. Also shown for comparison are the predicted spectral distributions computed from the models of Mihalas (1966) and Van Citters & Morton (1970) for B stars and the model of Schild, Peterson & Oke (1971) for Vega. It shows how the ultra-violet energy distribution varies with spectral type. However, not all the stars in Table I follow this temperature sequence according to their MK types. For example, the ultra-violet colours of 64 Ori (HD 41040) whose MK type is known to be B8 III match very well with those of B6 III (see Fig. 12 (a)). Fig. 12 (b) shows the flux distribution for four B7 stars, three of which are in close agreement but lie significantly higher than that of β C Mi (B7 V). There are several other cases.

The dispersion in ultra-violet colour with spectral type, depicted in Fig. 12 could be explained by errors in the V magnitudes of $\pm 0{\cdot}2$. However, this is unlikely since these are photoelectrically determined. Also, the deviant stars are slightly flatter in the ultra-violet so that a simple zero-point shift upward is not enough to explain the effect. It can be said that in general two stars of the same MK spectral type may differ in ultra-violet energy by an amount corresponding to as much as ± 2 subclasses. This effect appears to be more marked for the fainter stars.

(b) *Comparison with other observations*

There are very few published observations giving fluxes on an absolute scale below 3200 Å. Evans (1971) has measured absolute fluxes in the 1150–4000 Å range using a 13-in. telescope launched by an Aerobee rocket, but none of the

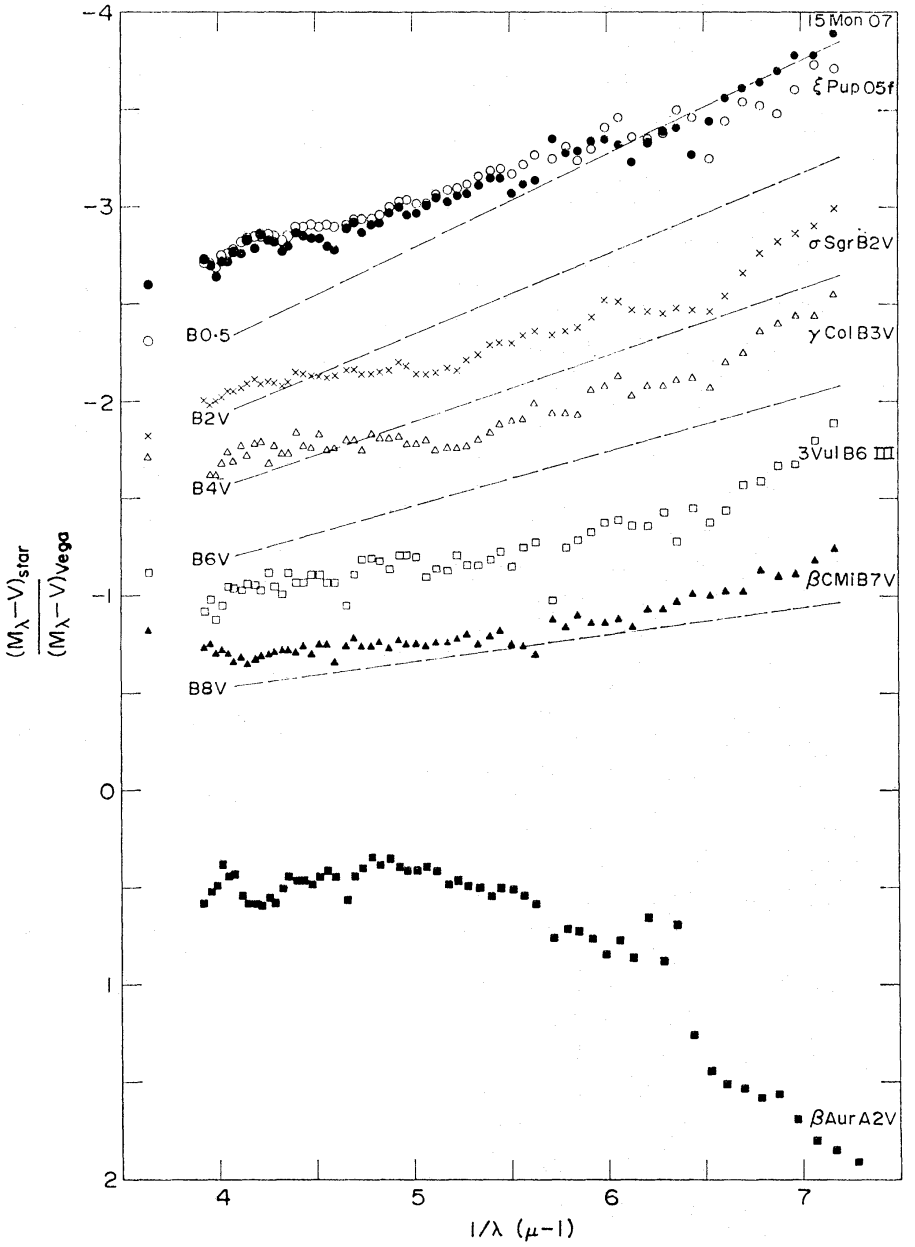

FIG. 11. *The variation of UV flux distribution with spectral type, fluxes given relative to Vega, A0 V. The dashed lines indicate spectral distributions computed from models.*

objects he selected are available among the data presently available from this experiment. Stecher (1970) has measured ultra-violet spectra of a few bright stars with 10 Å resolution and a comparison of his results with the present data is made for two hot stars ζ Pup and γ^2 Vel in Figs 13 and 14. The agreement is very satisfactory for wavelengths longer than about 1800 Å, but the present results give fluxes well above Stecher's at wavelengths below 1800 Å. This discrepancy can be understood in terms of atmospheric absorption, since the rocket observations of Stecher were carried out at a maximum altitude of 153 km, while the present telescope operates at 550 km above the Earth's surface.

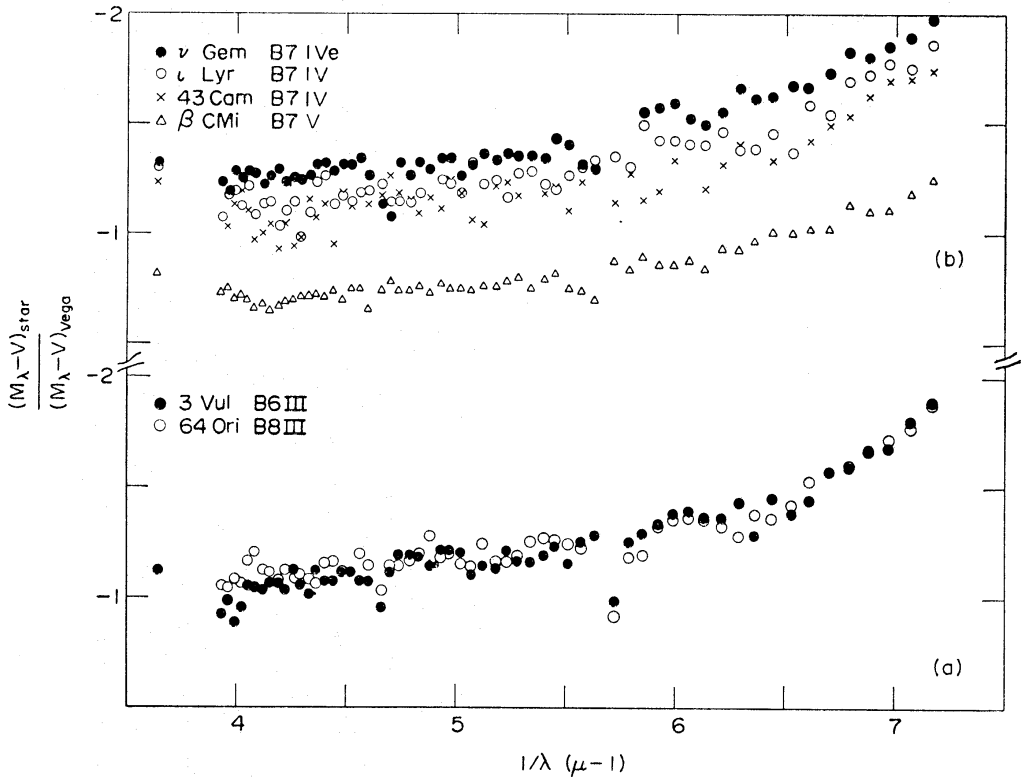

FIG. 12. *Variation in UV fluxes of stars of similar spectral type, (a) matching UV fluxes from different spectral types; (b) different UV fluxes from nominally the same spectral type.*

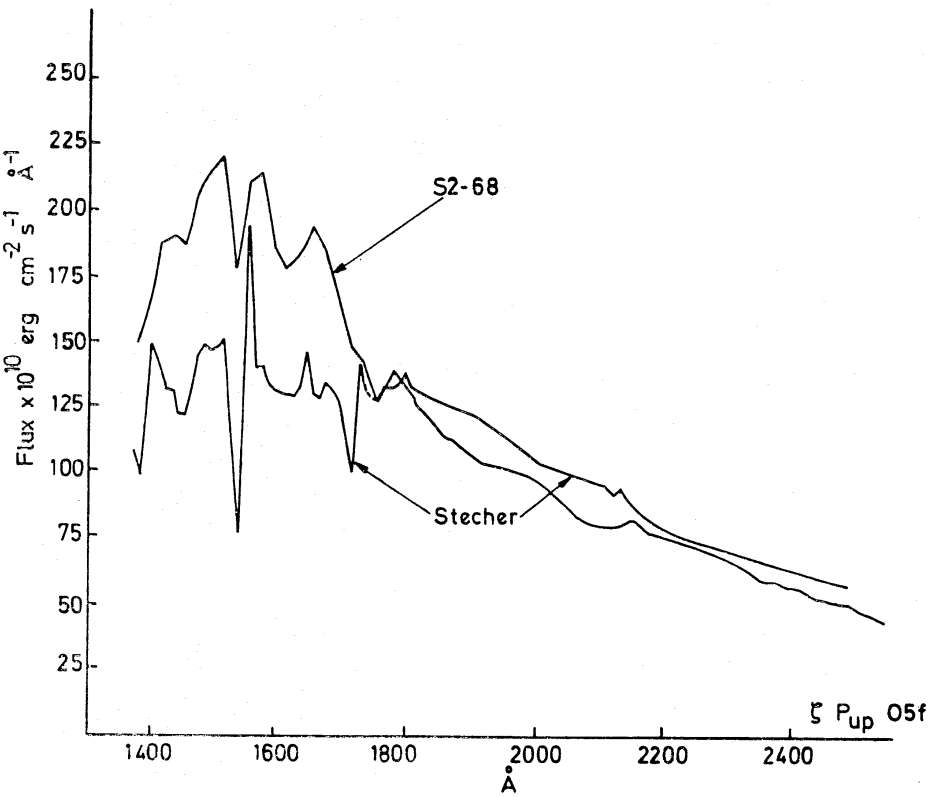

FIG. 13. *Comparison of absolute UV flux from ζ Pup O5f using the preliminary calibration of S2/68, with the rocket observations of Stecher.*

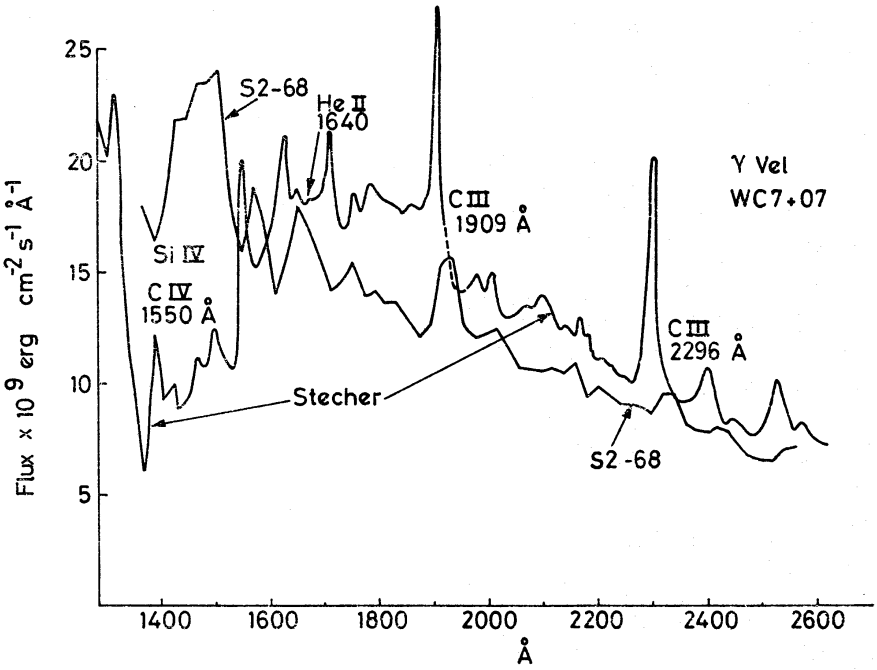

FIG. 14. *Comparison of absolute UV flux from γ^2 Vel WC7 + O7 using the preliminary calibration of S2/68, with the rocket observations of Stecher.*

(c) *Interstellar extinction*

The extinction curves for 16 pairs of stars are derived from the comparison of reddened and little reddened stars of the same nominal MK types as far as possible. The pairs of stars used for these curves are listed in Table II. It is to be noted that in some cases the reddened stars have been compared with more than one comparison star in order to reduce the error of the extinction curves due to uncertainty of the spectral type. The MK types are taken from the published catalogues. All the reddened stars except γ^2 Ori (HD 41117) and 67 Oph (HD 164353) are giants or main sequence stars, and have been compared with main sequence stars. In the case of supergiants no correction has been made for any difference due to luminosity class.

The extinction curves are normalized to $\Delta m = 0$ at $1/\lambda = 2{\cdot}64\ \mu^{-1}$, and to $\Delta m = 1$ at $1/\lambda = 4{\cdot}56\ \mu^{-1}$, where Δm denotes the magnitude difference. These reference wavelengths are defined respectively by the photometric channel and by the prominent feature in the ultra-violet extinction curve. This method of normalization has the following advantages over the usual normalization procedure, namely $A_V = 0$ and $E_{B-V} = 1$: (a) The wavelengths are more precisely defined than for broad band photometry, (b) no additional error is introduced due to uncertainty of E_{B-V}, and (c) it is better suited to study the extinction maximum which occurs near $1/\lambda = 4{\cdot}56\ \mu^{-1}$.

Four of the derived extinction curves are reproduced in Fig. 15(a) and show a pronounced structure dominated by the feature near $4{\cdot}56\ \mu^{-1}$. The four curves were selected to give the widest available range in spectral type (O6–B5) and luminosity class (V–Ia). Although there is some dispersion in the derived curves, the $4{\cdot}56\ \mu^{-1}$ feature is present in all four curves and is generally similar in shape and position. This indicates that its occurrence is independent of spectral type, or luminosity class and, hence, any possibility of this feature being intrinsic to the star or of circumstellar origin can be ruled out.

TABLE I

List of stars studied

HD/BD	Sp. type	V	$B-V$
50896	WN5	6·55	−0·15
68273 (γ^2 Vel)	WC7 + O7	2·22 var	−0·26
66811 (ζ Pup)	O5f	2·25	−0·28
54662	O5V	6·21	0·03
47839 (15 Mon)	O7	4·65	−0·24
57060	O9III	4·5	
−36° 12072	O	7·3	
53755	BoV	6·48	−0·05
48° 1339	Bo	6·5	
48434	BoIII	5·74	−0·02
165029	BoIII	6·5	
46328 (ξ^1 CMa)	Bo·5IV	4·33	−0·25
42953	B1	4·84	
54309	B1Ve	5·7	
60325	B1V	6·21	−0·04
39746	B1II	7·04	0·22
63578	B1V	5·20	−0·14
175191 (σ Sgr)	B2V	2·10	
41117 (χ^2 Ori)	B2Ia	4·63	0·28
164284 (66 Oph)	B2V	4·70	−0·04
44402 (ζ CMa)	B2·5 V	3·02	−0·20
40494 (γ Col)	B3IV	4·40	−0·18
61831	B3	4·90	−0·20
58343	B3V	5·2	−0·04
51283	B3II–III	5·28	−0·19
23° 3465	B3	6·51	
15° 3483	B3	6·54	
−33° 2700	B3	7·2	
164353 (67 Oph)	B5Ib	3·97	0·02
52092	B5	5·07	−0·17
171780	B5	6·11	−0·12
182255 (3 Vul)	B6III	4·89	−0·13
57815 (β CMi)	B7V	2·84	−0·10
45542 (ν Gem)	B7IVe	4·15	−0·11
49340 (43 Cam)	B7V	5·13	−0·13
178475 (ι Lyr)	B7IV	5·17	−0·11
41040 (64 Ori)	B8III	5·15	−0·11
40312 (θ Aur)	B9III	2·65	−0·09
47306	B9III	4·38	−0·02
172167 (α Lyr, Vega)	AoV	0·04	0·00
188228 (ϵ Pav)	AoV	3·95	−0·03
40183 (β Aur)	A2V	1·90	0·03

The 16 extinction curves derived from the star comparisons listed in Table II were combined into a single curve which is a weighted mean derived by weighting the individual curves by the reciprocal of their photometric errors. The result is reproduced in Fig. 15(b), the standard errors of the weighted mean curve being indicated by vertical bars. For comparison with OAO observations, the published extinction data of Bless & Savage (1972) normalized in the manner described above are also shown in Fig. 15(b). The mean rms dispersion of the present observations as well as those of OAO is about 20 per cent for wavelengths longer than 2190 Å and about 30 per cent for shorter wavelengths.

TABLE II

Pairs of reddened and comparison stars

Reddened star HD/BD	Comparison star HD
54662	47839
	66811
−36° 12072	66811
48434	54309
53755	54309
	42953
165029	57060
	42953
48°1339	57060
	42953
60325	46328
	42953
63578	42953
	46328
39746	54309
41117	44402
	40494
	51283
164284	42953
	145191
	44402
58343	44402
233° 465	40494
153° 583	40494
	51283
−33° 12700	44402
164353	52092
	171780

It can be seen from Fig. 15 that the extinction curves for χ^2 Ori and 67 Oph have a greater slope in the extreme ultra-violet than either the other two individual curves or the weighted mean curve. It is not possible to say, at this time, whether this is a real difference in the interstellar extinction properties or is due to intrinsic differences in the spectra of the reddened and comparison stars. The fact that both the stars referred to are supergiants indicates that the latter cause is a likely contributor to the observed dispersion. Indeed, the existence of significant errors due to mismatch of reddened and comparison stars is illustrated in Fig. 16 where the extinction curves for the same reddened star have been derived by comparison with two unreddened stars of nominally the same spectral type. This shows that the range of extinction curves as indicated by the quite large rms errors can be partly accounted for by the difficulty in matching the reddened and unreddened stars. It is clear that accurate extinction curves can only be derived if observations are available of a sufficiently large number of stars to allow the mismatch errors to be reduced to a level consistent with the photometric errors. The present sky-survey experiment, with its capability for observing a very large number of objects, is ideally suited to this purpose and the data will be used to derive accurate extinction curves and investigate any variations through the galaxy.

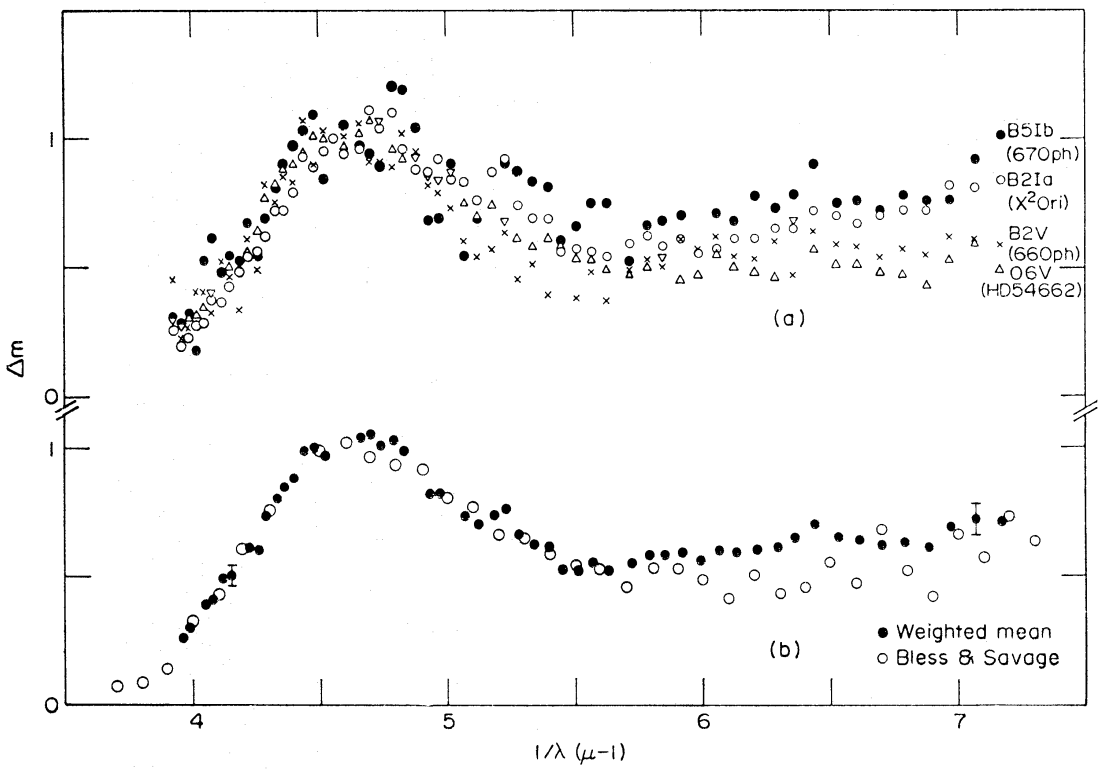

FIG. 15. *Interstellar extinction curves (a) S2/68 measurements on four reddened stars; (b) comparison of the mean S2/68 curve with the results of Bless and Savage.*

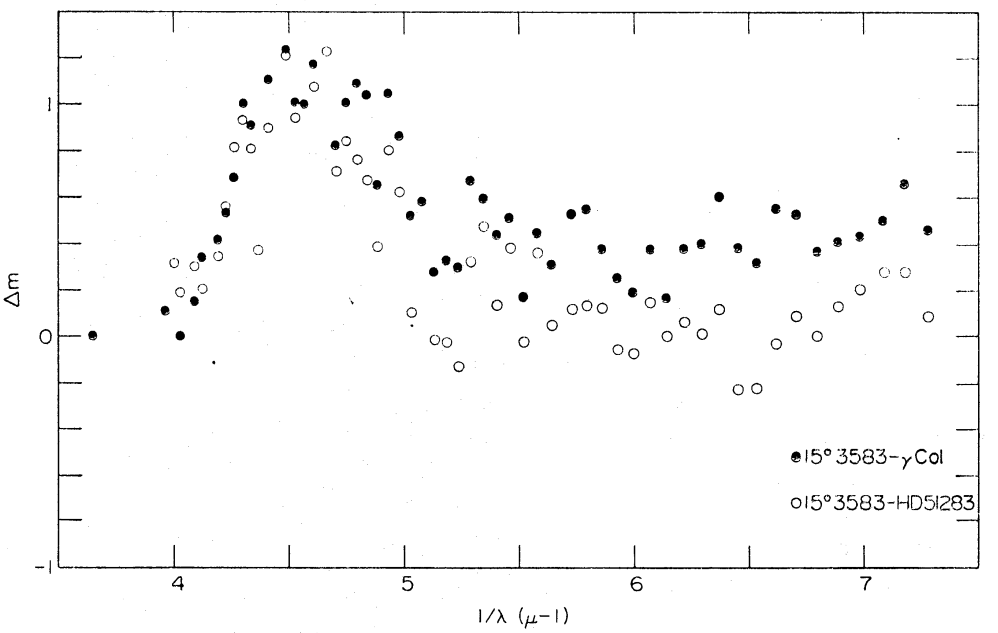

FIG. 16. *Interstellar extinction curves derived for the same reddened star using two different comparison stars of the same nominal spectral type.*

(d) *Wolf–Rayet Stars*

Two Wolf–Rayet stars have been covered in the data available on the quick-look tapes. These are the WC star γ^2 Vel and the WN star HD 50896; the spectrum of the former is reproduced in Fig. 14 and that of the latter in Fig. 17. The strongest emission lines in γ^2 Vel occur at 2296 Å and 1909 Å and are identified respectively

as the $2p^2\,{}^1D - 2s\,2p\,{}^1P^0$ and $2s\,2p\,{}^3P^0 - 2s^2\,{}^1S$ transitions of C III, while the corresponding transitions of the isoelectronic ion N IV are observed in HD 50896 at 1718 Å and 1488 Å. Both stars also show He II 1640 Å and C IV 1550 Å in emission, but the He II line is much stronger in HD 50896 and has an equivalent width of about 100 Å

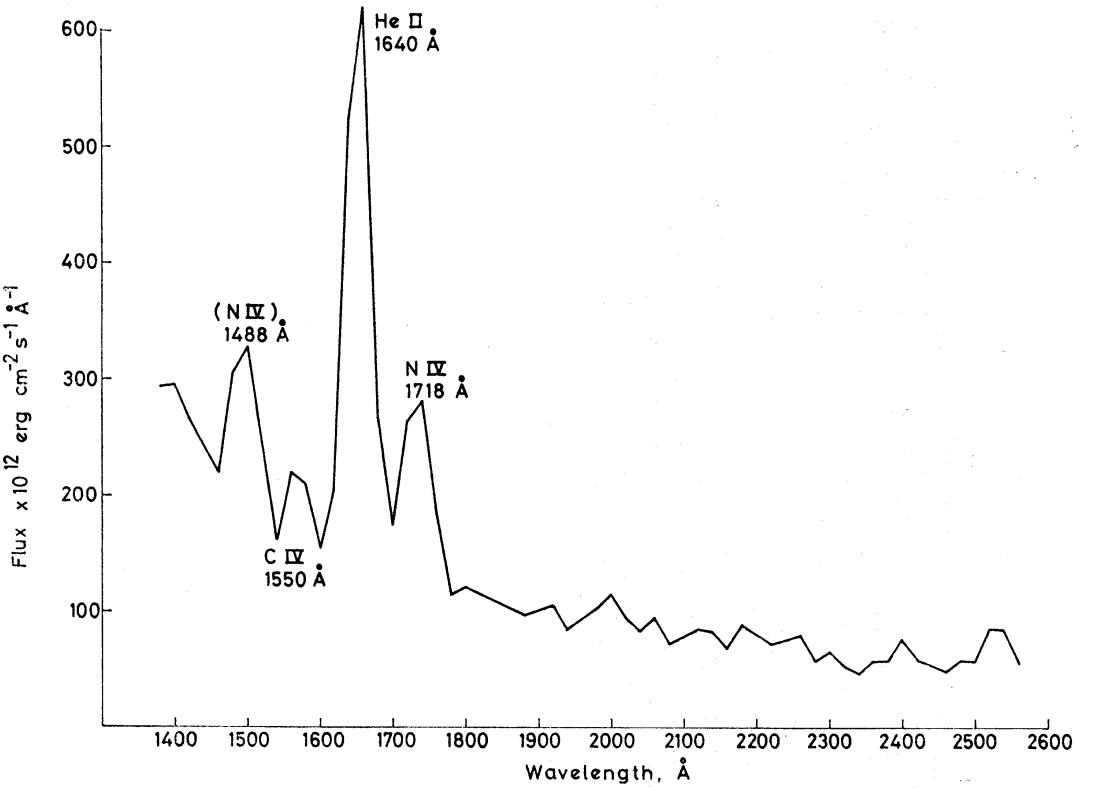

FIG. 17. *The absolute UV flux distribution from the WN5 star HD* 50896, $m_v = 6{\cdot}6$, *showing strong emission lines of He* II *and N* IV.

The $^1D - {}^1P^0$ and $^3P^0 - {}^1S$ transitions in C III and N IV occur between low-lying levels which are populated mainly by electron collisions. This is in contrast to the emission lines observed in the visible which are formed between highly-excited states and populated by recombination and cascade subsequent to photo-ionization. Since $^1D - {}^1P^0$ is a permitted transition whereas $^3P^0 - {}^1S$ is an inter-combination transition, the intensity ratio of the resulting lines is a function of electron density as well as electron temperature for the domain of interest. In the case of the solar spectrum, intensity ratios of permitted/intercombination lines in these Be-like ions have been used to derive electron densities since the electron temperature can be determined directly from the ionization balance (Jordan 1971). This is not possible in the present case where the ionization is produced by the Zanstra process. However, it is possible to derive a relationship between the electron density and electron temperature in the region emitting the lines from the observed ratio of their absolute fluxes.

In order to simplify these initial calculations, the line producing region is assumed to be uniform and optically thin. The latter condition is much less restrictive than would be the case if the medium were in LTE since it only requires generated photons to escape the layer without destruction. On this basis, the

equations of statistical equilibrium have been solved for both C III and N IV, allowing for the following processes:

Collisional excitation: $2s^2\ ^1S - 2p^2\ ^1D$; $2s^2\ ^1S - 2s\,2p\ ^3P^0$; $2s\,2p\ ^3P^0 - 2p^2\ ^1D$.
Collisional de-excitation: $2s\,2p\ ^3P^0 - 2s^2\ ^1S$.
Radiative decay: $2s\,2p\ ^3P^0 - 2s^2\ ^1S$; $2p^2\ ^1D - 2s\,2p\ ^1P^0$.

Other processes involving these terms are negligible over the range in N_e and T_e which is considered. The atomic data were taken from a review article by Gabriel & Jordan (1972) and solutions derived for the observed C III line flux ratio in γ^2 Vel and the observed N IV ratio in HD 50896. The resulting curves are displayed in Fig. 18 and indicate an approach towards LTE at the higher densities where the solution becomes temperature dependent only.

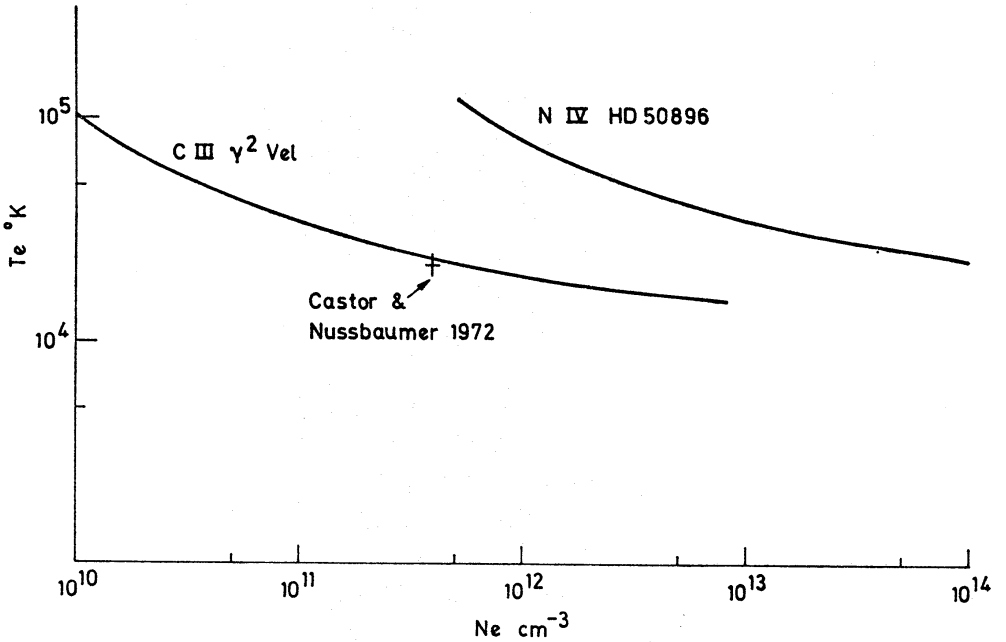

FIG. 18. *The locus of values of electron density N_e and electron temperature T_e which produce the observed emission lines intensity ratios, of C III in γ^2 Vel and N IV in HD 50896. The value of N_e and T_e calculated by Castor and Nussbaumer from the visible and UV spectra of γ^2 Vel is also shown.*

Castor & Nussbaumer (1972) have analysed the ultra-violet spectrum of γ^2 Vel obtained by Stecher in conjunction with its visible spectrum and derived the values of N_e and T_e which are also indicated in Fig. 18. This calculation assumes a uniform emitting region but does not require that the optical depth be small. The resulting values of N_e and T_e lie very close to the curve calculated from the present data alone.

It is clear from Fig. 18 that the region emitting the N IV lines in the WN star HD 50896 must have a higher electron temperature and electron density than the C III emitting region in the WC star γ^2 Vel. Advances beyond this preliminary calculation will require a more comprehensive and sophisticated model.

(e) *Large Magellanic Cloud*

The only extragalactic object so far identified on the quick look tapes is the Large Magellanic Cloud (LMC). It is observed weakly in channels A1, A3, and A4

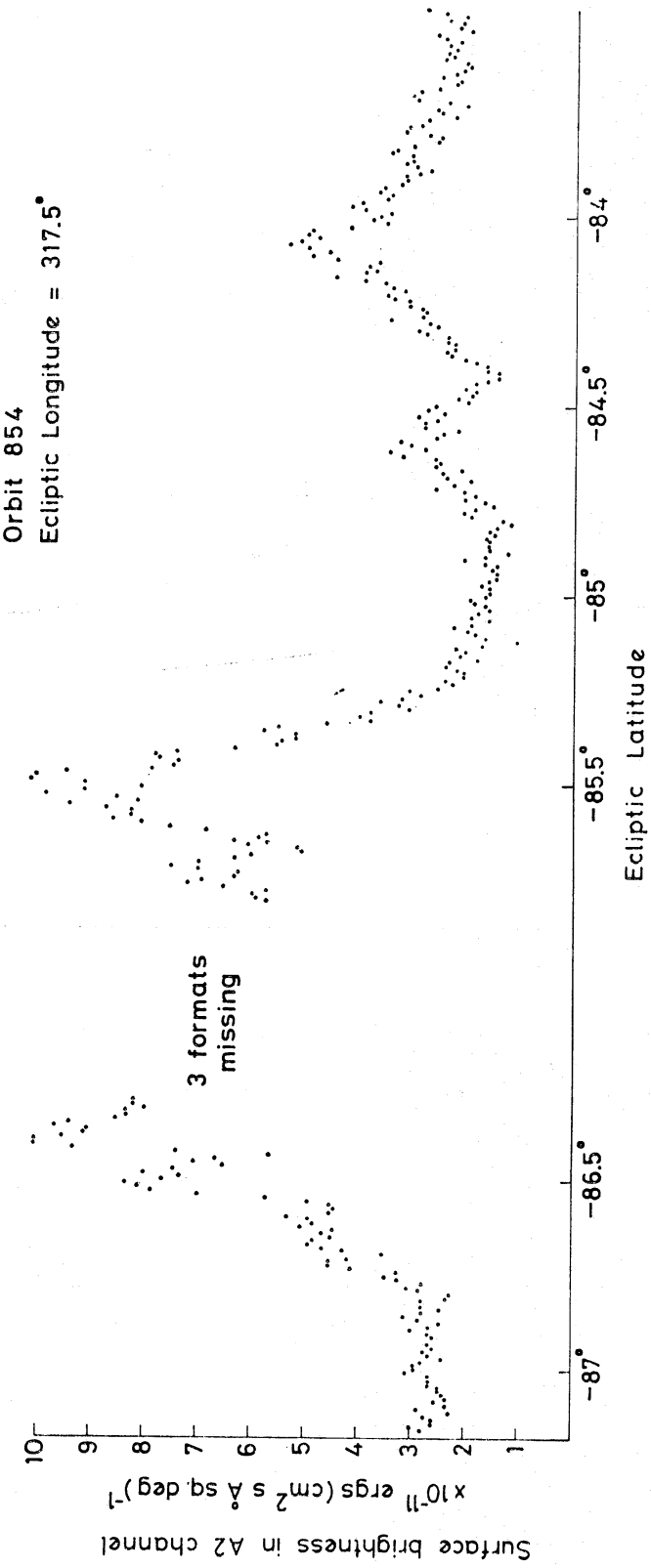

FIG. 19. *The signal in the A2 channel,* 1350–1760 *Å during one orbital scan through the Large Magellanic Cloud. Star signals on the same orbit were used to calculate ecliptic latitude and longitude, and the preliminary calibration data was used to calculate the surface brightness.*

but is much more prominent in A2, the short wavelength spectrophotometric channel. Since it is an extended source, position and wavelength are convoluted by the presence of the $12' \times 17'$ spectrometer entrance slot and the resulting flux is best regarded as a colour centred near 1500 Å with a bandwidth of $\sim$400 Å.

The signal in the A2 channel is shown in Fig. 19 for a scan through part of the LMC. The maximum signal is about four times the background and the LMC shows pronounced structure in its ultra-violet surface brightness. The character of the Cloud shows a marked difference from our own galaxy, being very much more intense at these short wavelengths.

Due to its proximity to the south ecliptic pole, the LMC is traversed a large number of times along slightly different orbits. It is planned to reduce data in order to provide a map of the surface brightness of the LMC at 1500 Å, and possibly also at 2000 Å, 2400 Å and 2800 Å, using the other three channels. This would be invaluable in view of the recent suggestion of spiral structure of the LMC, as shown in a far ultra-violet electronographic picture obtained by the recent Apollo 16 Moon mission (Carruthers 1972).

ACKNOWLEDGMENTS

The work owes much to the efforts of many colleagues in the collaborating groups, including P. J. Barker, P. S. Trowbridge, D. Booker, E. G. Higgins and C. S. Sutherland at the Rutherford Laboratory; H. E. Butler, G. E. Sudbury, D. H. Beattie and T. E. Purkins of the Royal Observatory Edinburgh; F. Beeckmans, R. Duysinx, S. Gardier, M. Henrist, J. Jamar, G. Marette of the Institute d'Astrophysique, Liège; A. Danks and G. Houziaux of the Université d eMons; M. J. Esten of University College London; and W. M. Burton of the Astrophysics Research Unit, Culham.

The UK prime contractor responsible for the structure, optics, integration and test of the experiment was Hawker Siddeley Dynamics, Stevenage, where the team was led by P. A. G. Clapp. The Belgian contractor, responsible for the detector system, was ETCA, Charleroi, where the team was led by A. Vuye. The spacecraft was the responsibility of ESTeC, Holland, where the team was led by T. E. Curl; we are also indebted to the experiment engineer J. Kingdon and the project scientist J. van Boeckel. Orbital operations are conducted by a team under B. M. Walker at ESOC, Germany.

C. Jamar, D. Macau, J. P. Macau, D. Malaise and A. Monfils, Institute d'Astrophysique, Liège; L. Houziaux, Université de Mons; C. M. Humphries, K. Nandy and G. I. Thompson, Royal Observatory, Edinburgh; R. G. Fowler, I. S. K. Gardner and H. Wroe, Rutherford Laboratory, Chilton; R. G. Evans, Astrophysics Research Division, SRC/RSRS, Culham; A. Boksenberg and R. Wilson, University College, London.

REFERENCES

Bless, R. C. & Savage, B. D., 1972. *Astrophys. J.*, **171**, 293.
Boksenberg, A. & Gerard, J. C., 1973. *J. geophys. Res.*, in press.
Carruthers, G. R., 1972. *Sky Telesc.*, **44**, 9.
Castor, J. I. & Nussbaumer, H., 1972. *Mon. Not. R. astr. Soc.*, **155**, 293.
Evans, D. C., 1971. The Scientific Results from *OAO-2 NASA SP-310*, 347.
Gabriel, A. H. & Jordan, C., 1972. *Case studies in atomic collision physics*, p. 211. eds McDaniel & McDowell, North Holland.

Hanson, W. B. & Sanatini, S., 1970. *J. geophys. Res.*, **75**, 5503.
Hanson, W. B., Sterling, D. L. & Woodman, R. S., 1972. *J. geophys. Res.*, **77**, 5530.
Jordan, C., 1971. *Highlights of Astronomy*, p. 519, ed de Jager, International Astronomical Union.
Mihalas, D., 1966. *Astrophys. J. Suppl.*, **13**, 1.
Oke, J. B. & Schild, R., 1970. *Astrophys. J.*, **161**, 1015.
Schild, R., Peterson, B. M. & Oke, J. B., 1971. *Astrophys. J.*, **166**, 95.
Stecher, T. P., 1970. *Astrophys. J.*, **159**, 553.
Tilgner, B., 1971. *Sci. Tech. Rec.* (ELDO/ESRO), **3**, 567.
Van Citters, G. W. & Morton, D. C., 1970. *Astrophys. J.*, **161**, 695.